



Pushing the boundaries
of chemistry?
It takes
#HumanChemistry

Make your curiosity and talent as a chemist matter to the world with a specialty chemicals leader. Together, we combine cutting-edge science with engineering expertise to create solutions that answer real-world problems. Find out how our approach to technology creates more opportunities for growth, and see what chemistry can do for you at:

evonik.com/career



Lighting the Path: Light Delivery Strategies to Activate Photoresponsive Biomaterials In Vivo

Samuel Pearson,* Jun Feng, and Aránzazu del Campo*

Photoresponsive biomaterials are experiencing a transition from *in vitro* models to *in vivo* demonstrations that point toward clinical translation. Dynamic hydrogels for cell encapsulation, light-responsive carriers for controlled drug delivery, and nanomaterials containing photosensitizers for photodynamic therapy are relevant examples. Nonetheless, the step to the clinic largely depends on their combination with technologies to bring light into the body. This review highlights the challenge of photoactivation *in vivo*, and presents strategies for light management that can be adopted for this purpose. The authors' focus is on technologies that are materials-driven, particularly upconversion nanoparticles that assist in "direct path" light delivery through tissue, and optical waveguides that "clear the path" between external light source and *in vivo* target. The authors' intention is to assist the photoresponsive biomaterials community transition toward medical technologies by presenting light delivery concepts that can be integrated with the photoresponsive targets. The authors also aim to stimulate further innovation in materials-based light delivery platforms by highlighting needs and opportunities for *in vivo* photoactivation of biomaterials.

1. Introduction

Light-responsive biomaterials are becoming a prominent element of biomedical research. Light as a cue is widely available, easily controllable, and orthogonal to many biological and chemical processes, making it highly appealing for imparting precise control over biomaterial properties and function. Light-responsive carriers for drug delivery^[1] and light-responsive


hydrogels that provide instructive signals to embedded cells^[2] are examples that have been explored extensively *in vitro*.^[3] The potential of these systems to mature into advanced therapeutic formats is recognized from initial *in vivo* demonstrations. In mice, for example, injectable photoresponsive drug delivery vehicles that sequentially release shRNA and a chemotherapeutic on command have improved the efficacy of chemotherapy,^[4] and implanted photoresponsive hydrogels have permitted light-triggered control over cellular responses for improved regenerative outcomes.^[5]

Despite the clear therapeutic potential, most of the investigated photoresponsive biomaterials require UV light for photoactivation, which hampers transfer to scenarios deep within the body. Beyond phototoxicity issues associated with UV light, absorption and scattering by biological tissue rules out the possibility to activate photochemical or photobiological

processes even just below the skin by simply irradiating the organism from the outside. The biomaterials community has therefore sought alternatives to overcome the problem of light attenuation in the body. On the photochemistry side, molecular designs permitting photoactivation at wavelengths that approach or lie in the more tissue-transparent "first therapeutic window" (700–900 nm)^[6] are in development, as recently reviewed by Rapp and DeForest^[7] and by the Klan workgroup.^[8] Photoresponsive groups that absorb at longer-wavelength visible (vis) and near-infrared (NIR) wavelengths (e.g., BODIPY^[9] and red-shifted coumarins^[10] and azobenzenes^[11]) have been developed as photoactivatable groups^[12] and photoswitches^[13] for bioactive species, photocleavable crosslinks for degradable hydrogels,^[14] and photoinitiators^[15] for acrylate and thiol-ene polymerizations. From a photophysics point of view, two-photon (2P) excitation processes^[16] have been used to activate UV-sensitive groups with NIR light, and wavefront shaping approaches have overcome some of the scattering effects of tissue.^[17] From a bioelectronics perspective, implantable light sources^[18] are progressing, mostly linked to the optogenetics community.

The materials community has also developed alternative approaches to solve the limited penetration of light into tissue. These technologies can be combined with photoresponsive systems, like chromophores or optogenetically modified cells, to develop *in vivo* applicable therapeutic platforms. Upconversion nanoparticles (UCNPs) for example can activate UV- and vis-responsive reactions using NIR light. The upconversion process

S. Pearson, J. Feng,^[†] A. del Campo
INM – Leibniz Institute for New Materials
Campus D2 2, 66123 Saarbrücken, Germany
E-mail: Samuel.Pearson@leibniz-inm.de;
Aranzazu.delCampo@leibniz-inm.de
J. Feng, A. del Campo
Chemistry Department
Saarland University
66123 Saarbrücken, Germany

 The ORCID identification number(s) for the author(s) of this article can be found under <https://doi.org/10.1002/adfm.202105989>.

© 2021 The Authors. Advanced Functional Materials published by Wiley-VCH GmbH. This is an open access article under the terms of the Creative Commons Attribution-NonCommercial License, which permits use, distribution and reproduction in any medium, provided the original work is properly cited and is not used for commercial purposes.

^[†]Present address: Institut für Chemie und Biochemie – Organische Chemie, Freie Universität Berlin, Takustrasse 3, 14195 Berlin, Germany

DOI: 10.1002/adfm.202105989

is significantly more efficient than 2P excitation and does not require high energy femtosecond pulsed lasers.^[19] UCNP have successfully transitioned from initial in vitro demonstrations^[20] to in vivo platforms for minimally-invasive neuronal optogenetics,^[21] non-neuronal optogenetic therapy,^[22] light-triggered drug delivery^[23] and gene therapy,^[24] and photodynamic therapy (PDT).^[25] Complementary to upconversion technology, implantable optical waveguides that can deliver light from an external source into the body also show promise for the activation of biomaterials in vivo. Optical waveguides are widespread in optogenetics research, but have been rarely used to activate photoresponsive materials.

This review highlights light management strategies (Figure 1a,b) that have been used to perform in vivo photo(bio)chemistry (i.e., photoactivation of an in vivo “target” species) in different fields (Figure 1c–f). Our aim is to contribute to the light-responsive biomaterials community by presenting light management strategies that could facilitate photoactivation in the human body. Our focus is on materials-assisted light management approaches that could be integrated with photoresponsive biomaterials. More concretely, the review is divided into five sections. After this introduction, Section 2 describes the challenges of delivering photons through tissue in terms of limited penetration depth and skin exposure limits, and defines irradiance values that can be safely achieved at a chosen depth. The next two sections are then devoted to the two photoactivation approaches which we classify as either “direct path” (Figure 1a, Section 3) or “clearing the path” (Figure 1b, Section 4) strategies. We define direct path strategies as those in which externally-produced light passes directly through tissue before reaching an in vivo target or a transducing material co-located with the target. The feasibility of direct path photoactivations is therefore dictated primarily by the light-tissue interactions outlined in Section 2. Section 3 emphasizes direct path strategies utilizing transducing biomaterials that can be integrated with photoactivatable targets and convert more penetrating long wavelength photons into shorter wavelength photons at the target site. UCNP-assisted photoactivations dominate this section, as they offer significant improvements in photoactivation depth without complicated hardware requirements. Even with materials assistance, however, direct path photoactivations are still restricted to centimeter-scale depths, motivating the development of optical waveguides (Section 4) that “clear the path” between the external light source and deeper in vivo targets (Figure 1b). The feasible depth of waveguide-based photoactivation is predominantly defined by light-material interactions and the waveguide design. The design, material properties, and fabrication of biomedical waveguides are described, and their applications for in vivo photoactivations are discussed according to the role played by the waveguide. Section 5 summarizes the state of the art based on the prior sections, and provides an outlook on the exciting developments and translational challenges that are imminent in the field of in vivo light delivery for activation of photoresponsive biomaterials.

We want to make the reader aware of the following recent reviews addressing some of the concepts here, but from different perspectives. In 2017 Yun and Kwok provided a broad, comprehensive overview of light in diagnosis, therapy, and surgery,^[26] and more recently the same group reviewed biomaterial-based waveguides^[27] and implantable/wearable photonic biomedical devices.^[28] Reports addressing progress in the

synthesis of UCNP,^[29] and a roadmap for the translation of UCNP to medical applications,^[30] have been followed by a recent overview of UCNP in optogenetics research.^[31]

2. The Challenge of In Vivo Light Delivery

2.1. Light-Matter Interactions Limit Light Penetration Depth in Tissue

Light is attenuated as it passes through materials, including tissues, mainly by scattering and absorption. Scattering, which involves the interaction of photons with matter without the species being excited into a higher electronic state,^[32] can be essentially viewed as a deflection of photons from their original trajectory. Scattering is highly wavelength-dependent, and becomes more and more prominent as wavelength decreases. Absorption involves the capture of a photon by an absorbing species, elevating the absorber into a higher electronic or vibrational state. The excited species can then return to the ground state via a variety of processes. The absorption of light by tissue is largely determined by the concentrations of a handful of key species—melanin, hemoglobin (and its degree of oxygenation), fat, and water, and to a lesser extent the yellow pigments bilirubin and β -carotene—each of which make their own wavelength-dependent contribution to the total absorption (Figure 2a).^[33]

The contributions of scattering and absorption as light passes through different tissue types have been compiled by Jacques^[33] and continue to be updated with more accurate in vivo data.^[34] The irradiance E (W cm^{-2}) of a particular wavelength that can be achieved at depth x through a given tissue can be estimated from the effective attenuation coefficient, μ_{eff} (cm^{-1}) which is a summation of the scattering and absorption coefficients ($\mu_{\text{eff}} = \mu_s + \mu_a$):

$$E = E_0 e^{-\mu_{\text{eff}} x} \quad (1)$$

Values for μ_{eff} across wavelengths of interest are shown in Figure 2a for brain tissue.^[35] The main absorbing species at each wavelength are labeled. Note that the scattering coefficient, μ_s , is close to 100 cm^{-1} at 350 nm based on literature values,^[35] and remains a significant contributor to attenuation across the shown wavelengths. The lines for fully oxygenated and fully deoxygenated tissue show the non-negligible effect that the oxygenation state of hemoglobin plays on absorption. Figure 2b converts the attenuation coefficient data at 72% oxygen saturation from Figure 2a into penetration depth, L_e , defined as the depth at which irradiance declines to $1/e$ ($\approx 37\%$) of its initial value. Figure 2b also shows depths at which the irradiance declines to 10%, 1%, and 0.1% of its incident value to show the substantial rate at which light intensity decays with increasing depth. Despite relatively large variability in literature values for μ_{eff} used to compile such plots,^[33] the empirical relationships allow us to estimate the depth at which a given in vivo photoactivation is likely to be feasible by direct irradiation. We see that maximum penetration depth ($L_e \approx 3.5\text{--}4.5 \text{ mm}$) occurs in the region 700–900 nm, which is referred to as the “first NIR window” or the “first therapeutic window” (Figure 2b).^[6] Choosing a light-driven process which can be activated efficiently by photons in this wavelength region may

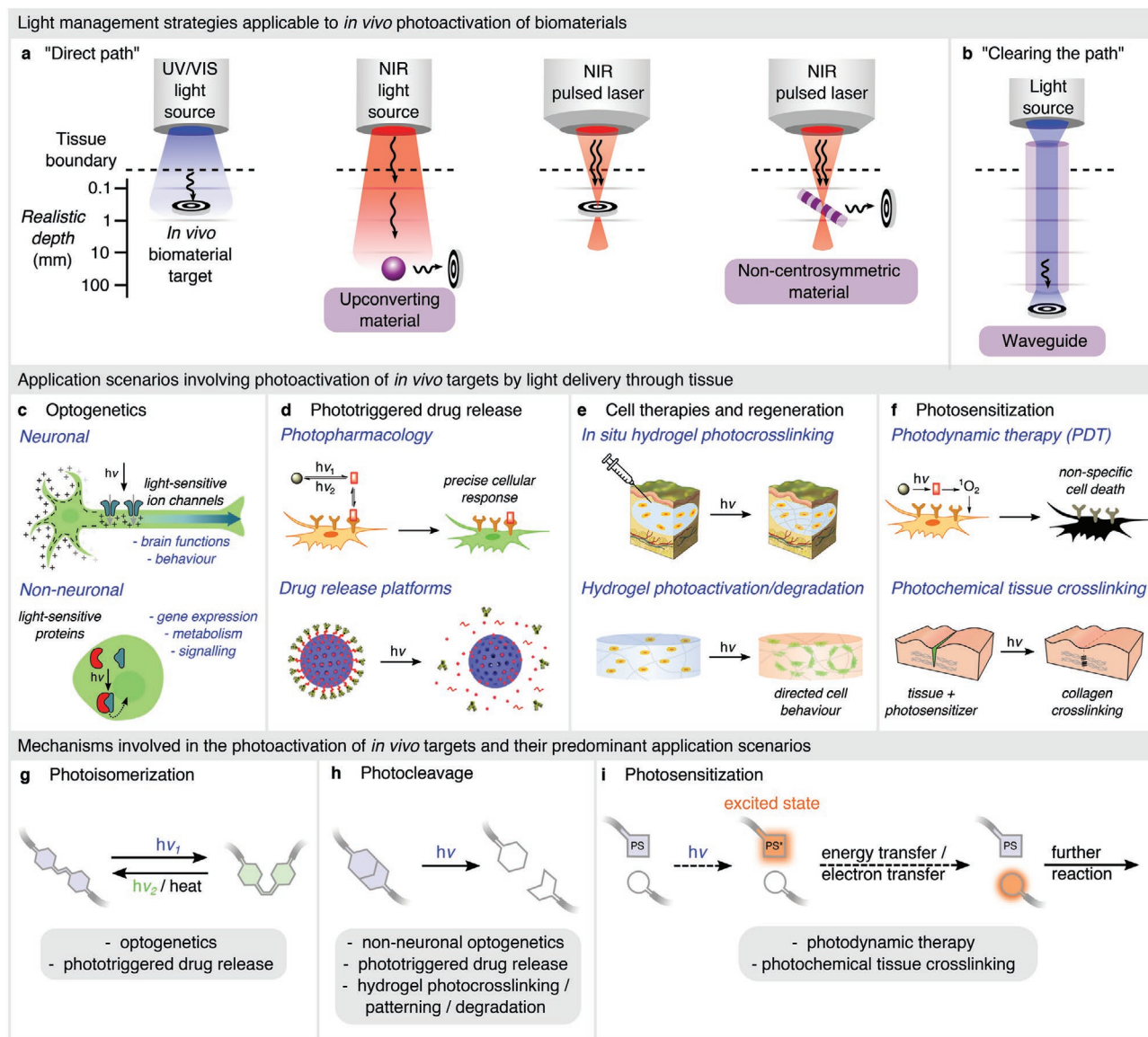


Figure 1. Depiction of a) direct path (Section 3) and b) clearing the path (Section 4) light management strategies used for photoactivation of *in vivo* targets covered in this review. The *in vivo* applications scenarios in which photoactivation have been used are: c) Manipulation of cellular function by optogenetics (Section 3.3.1); d) light-triggered drug (de)activation and release (Section 3.3.2). Adapted with permission.^[36] Copyright 2014, The American Chemical Society, Copyright 2020, Nature Publishing Group; e) photocrosslinking, photopatterning, and photodegradation of hydrogels for cell therapies and regenerative medicine (Section 3.3.3). Adapted with permission.^[37] Copyright 2011, American Association for the Advancement of Science; and f) photosensitization, namely PDT (Section 3.3.4). Adapted with permission.^[36a] Copyright 2014, The American Chemical Society. The three types of photochemical processes that underpin light-based therapies and biomaterial photoactivations are g) photoisomerization, h) photocleavage, and i) photosensitization.

give an effective penetration depth up to 2 orders of magnitude higher than one driven by UV light for example—from hundreds of microns to several centimeters. The “window,” however, is far from transparent, with only a tiny fraction (<0.1%) of photons reaching a depth beyond several centimeters. As we see in the next section, the brute force compensation strategy of increasing the number of incident photons is limited by potential photochemical or photothermal damage to overlying tissue.

The vast majority of photochemical reactions implemented in photoresponsive materials require UV and shorter vis

wavelengths. Photoresponsive groups in the NIR therapeutic window are in high demand, but are often accompanied by complicated syntheses and solubility issues due to the need of extended conjugated systems.^[7,8] A mismatch therefore exists between the wavelengths of the optical window and the available photoresponsive groups. This gap can be bridged by upconversion materials (Section 3) generating short wavelength photons from long wavelength ones, and waveguides (Section 4) offering a clear path for deeper light delivery irrespective of wavelength.

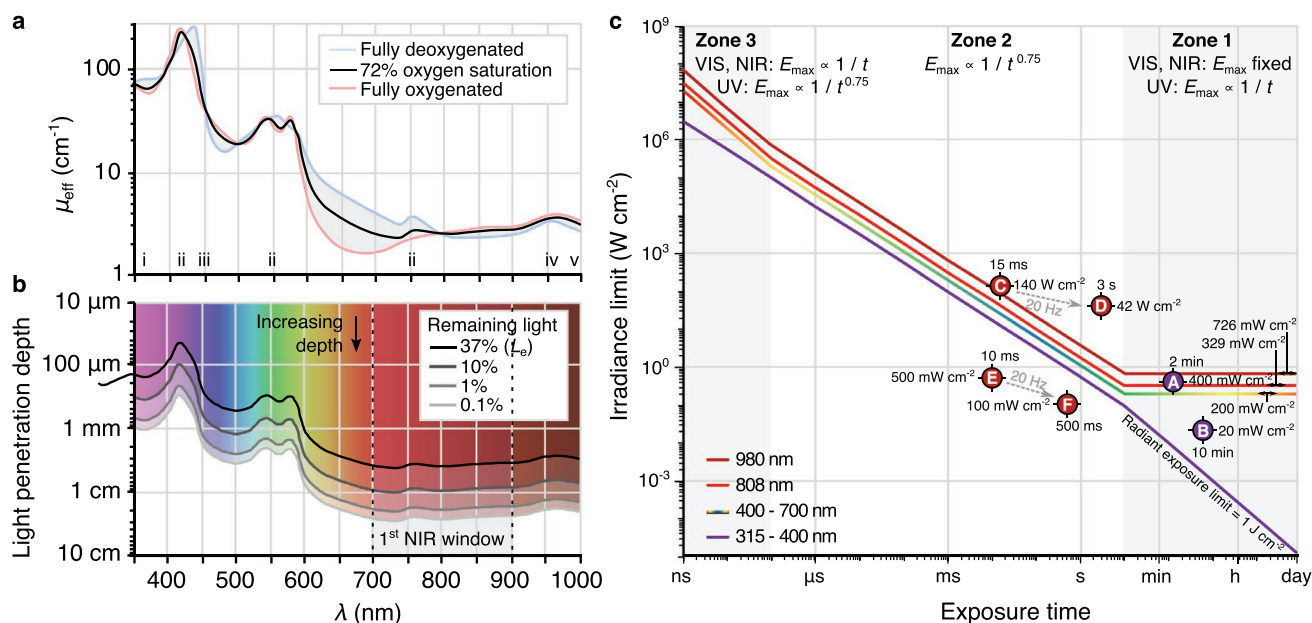


Figure 2. a) Effective attenuation coefficient for brain tissue at 72% oxygen saturation, full deoxygenation, and full oxygenation. Adapted with permission.^[35] Copyright 2015, John Wiley & Sons. The labels i–v correspond to the wavelengths at which the main absorbing species in tissue have absorbance maxima: i) melanin (negligible contribution here), ii) hemoglobin (multiple maxima, with the effect of oxygenation clear from the plot), iii) yellow pigments (negligible here), iv) fat, and v) water. b) Corresponding penetration depth L_e , defined as the depth at which the irradiance declines to $1/e$ ($\approx 37\%$) of its initial value, as a function of wavelength from the data in (a). Lines representing the depth at which light reaches 10%, 1%, and 0.1% of incident intensity are also shown. c) Maximum permissible exposure (MPE) for skin as a function of exposure time. Colored lines show the irradiance limits from reported data^[38] for human skin at wavelengths most relevant to this review. Key examples of in vivo irradiances and durations from relevant literature are shown at points color-coded according to wavelength. Point A = uncaging of photocaged DNA in subcutaneously-injected vesicles using 365 nm light.^[39] Point B = uncaging of bioactive ligands in a subcutaneously implanted hydrogel using 351 nm light in live mice.^[5] Point C = single pulse of NIR (980 nm, 15 ms) and Point D = average irradiance of the corresponding pulse train (20 Hz, 3 s duration) used for optogenetic activation of deep brain neurons in mice through intact mouse skull and brain using injected UCNP.^[2] Point E = single NIR pulse (980 nm, 10 ms) and Point F = average irradiance of the pulse train (20 Hz, 500 ms duration) in optogenetic experiments performed with assistance of an UCNP-containing microneedle in live mice.^[40]

2.2. Maximum Permissible Exposure Defines the Ceiling for Safe Irradiances

Photodamage occurs through the excessive absorption of photons by tissue within a given timeframe. Excited species generated by absorbed UV photons may induce photochemical changes like DNA cleavage and reactive oxygen species (ROS),^[41] while heat generated as excited species relax to the ground state is the predominant damage mechanism induced by longer wavelengths.^[42] The irradiances which can be safely delivered for photoactivation of in vivo targets are therefore limited by these processes. The maximum permissible exposure (MPE) for skin and eyes provides a quantitative limit for light delivery approaches in deep tissue targets.^[38] Figure 2c summarizes the MPE for skin, which we will denote E_{max} (in W cm⁻²), as a function of exposure duration for wavelengths most relevant to this review; UV (315–400 nm), vis (400–700 nm), and NIR (808 and 980 nm). Throughout the review, we will state irradiance values E reported in key papers as a proportion of the irradiance limit E_{max} for that exposure duration (in brackets). This E/E_{max} value conveniently indicates the clinical applicability of the applied irradiances based on current guidelines. Figure 2c shows that for all exposure durations, irradiance limits from UV to NIR wavelengths increase with

increasing wavelength. This, combined with their greater penetration depths, explains why longer wavelengths are preferred for driving in vivo photoprocesses.

The time domain $t \geq 10$ s (denoted Zone 1) is the most relevant to typical phototherapy applications using continuous irradiation. Here, the exposure limit of UV (315–400 nm) is defined by a fixed radiant exposure value (i.e., energy per unit area) of 1.0 J cm⁻², meaning that E_{max} varies inversely with exposure duration. Longer exposure periods are therefore only permitted if irradiance is reduced. Skin exposures for direct activation using UV light in vivo are often well above E_{max} , since honoring this limit typically delivers too few photons for successful photochemistry at subcutaneous depths (i.e., just a few hundred microns in mice). For context, a subcutaneously-injected vesicle “nanofactory” required 2 min of 365 nm irradiation at 400 mW cm⁻² (Figure 2c, Point A) to activate photocaged DNA and induce production of fluorescent protein in mice.^[39] This irradiance significantly exceeds the MPE for human skin of $E_{\text{max}}(2 \text{ min}) = 8.3 \text{ mW cm}^{-2}$ ($E/E_{\text{max}} = 48$), and highlights the formidable barrier to safely translating such direct UV-activated systems to humans given that human skin is many times thicker than mouse skin. In a biomaterial example, Lee et al.^[5] used 10 min of 351 nm radiation at 20 mW cm⁻² (Figure 2c, Point B, $E/E_{\text{max}} \approx 12$) to activate a photoresponsive

hydrogel implanted subcutaneously in live mice. An absence of discernible skin photodamage or adverse effects was noted despite exceeding E_{\max} , but translation to humans would again be impeded by the higher skin thickness. In contrast to UV light, the E_{\max} values for vis and NIR wavelengths are time-independent in Zone 1. vis and NIR wavelengths can therefore be delivered for long (hours) durations at the irradiance limit, and the radiant exposure (total energy delivered) is allowed to climb accordingly. This creates a strong incentive to develop vis and NIR-based alternatives to current UV-driven photoprocesses requiring photoactivation periods that fall in Zone 1 (i.e., >10 s exposure duration).

Zone 2, from 100 ns to 10 s exposure duration, shows irradiance limits varying inversely with $t^{0.75}$ for all wavelengths. Neuronal optogenetic experiments, typically performed with light pulses in the milliseconds range, are good examples of in vivo processes falling in Zone 2. Critically, when a sequence of multiple pulses (also known as “pulse train”) is delivered within a certain time period, the irradiance of each individual pulse, denoted $E(t_{\text{pulse}})$, and the average irradiance over the time from the first to the last pulse $E_{\text{average}}(t_{\text{total}})$ should both conform to the irradiance limit. For example, a 10 ms pulse of vis light at 10 W cm^{-2} is well below $E_{\max}(10 \text{ ms}) = 35 \text{ W cm}^{-2}$, but a series of such pulses delivered at 50 Hz for 1 second gives $E_{\text{average}}(1 \text{ s}) = 5 \text{ W cm}^{-2}$ which exceeds $E_{\max}(1 \text{ s}) = 1.1 \text{ W cm}^{-2}$. In vivo optogenetic experiments performed on mice by Chen et al.^[21] used 15 ms NIR pulses (980 nm, 140 W cm^{-2} , 20 Hz) for 3 s, meaning the single pulse irradiance (Figure 2c, Point C) slightly exceeded the limit: $E/E_{\max}(15 \text{ ms}) = 140 \text{ W cm}^{-2}/93 \text{ W cm}^{-2} = 1.5$. The average irradiance (Figure 2c, Point D) also exceeded the MPE, with $E_{\text{average}}/E_{\max}(3 \text{ s}) = 24$. This ground-breaking paper detailed in Section 3.2.1 demonstrated that the significant heating effect associated with these irradiances did not cause photothermal damage. Light doses exceeding the guidelines in Figure 2c may therefore still prove acceptable, and safe light doses for each clinical scenario need to be individually assessed. In contrast, successful photoactivation was achieved at single pulse and average irradiances well below E_{\max} (Figure 2c, Points E and F) by Shi and co-workers^[40] for optogenetics deep in the brains of live mice using 10 ms NIR pulses (980 nm, 500 mW cm^{-2} , 20 Hz over 500 ms). In this case, light delivery was facilitated by light guidance from the implanted device, while the system of Chen et al. enjoyed no such benefit and therefore required much higher irradiances for successful photoactivation at comparable depths.^[21] This hybrid example between “direct path” and “clearing the path” light delivery^[40] hints at the benefits offered by waveguides detailed in Section 4.

In Zone 3 (<100 ns), the irradiance limit varies inversely with exposure duration for vis and NIR wavelengths, while the irradiance limit for UV wavelengths follows Zone 2. Limits for pulses even shorter than 1 ns can be assumed to follow Zone 3 trend lines.^[38] Non-linear optical processes such as 2P activation and second harmonic generation (SHG) typically require high irradiance, ultra-short pulses defined in Zone 3. The need for the target species to capture two photons almost simultaneously requires very high irradiance at the focal plane, which restricts 2P processes to much shallower penetration depths than one-photon (1P) processes. In some cases, transparent

windows are used to avoid excessive scattering of NIR photons en route to the focal plane, which is typically at just a few hundred microns depth.^[43] The advantage of 2P activation using a focused NIR beam is that the beam footprint at the tissue surface is much larger than at the focal plane, meaning that the surface irradiance is typically orders of magnitude lower than at the target depth.

3. Direct Path Light Delivery

In vivo photoreactions can be achieved using 1P or 2P excitation of the target through tissue (Figure 3a,b), or by using transducing materials that mediate in situ conversion of low energy incident photons into higher energy secondary photons which then excite the nearby target (Figure 3c,d).

Most photoprocesses are activated by absorption of one photon, typically in the UV/vis region. In 2P absorption, the molecule absorbs two photons in the NIR region almost simultaneously to reach the excited state.^[32] This requires powerful femtosecond pulsed lasers with NIR irradiances in the MW cm^{-2} to GW cm^{-2} range,^[48] which limits clinical applicability of 2P excitation. As an alternative to direct 1P or 2P absorption of photons delivered from outside the body, a transducing material introduced in the vicinity of the photoactivatable target can be used to pool the energy of NIR photons and produce a single photon of higher energy (UV/vis wavelength) for target excitation. Such material-assisted strategies (Figure 3c,d) allow 1P photochemistry to be performed at greater depth and lower risk by capitalizing on the higher penetration and less cellular photodamage of long-wavelength photons. In doing so, activation depth for UV/vis processes can increase from hundreds of microns to several centimeters while minimizing photodamage to overlying tissue. Although penetration depth is increased, a relatively small proportion of NIR photons delivered to transducing materials are upconverted into higher energy photons. Figure 3e compares the photoactivation strategies described in Figure 3a–d in terms of the approximate irradiation time required to reach 1% conversion in a model photoreaction, with the average irradiance held constant. Activation of the 1P and UCN systems is shown using continuous light sources as is typical in literature, while the 2P and SHG photoactivations are depicted under typical pulsed laser irradiation regimes. The irradiation times vary by orders of magnitude, increasing in the order $1\text{P} < \text{UCNP} < 2\text{P} \approx \text{SHG}$ unless very high pulse irradiances are used for the 2P and SHG processes. Although the irradiation time for the UCN system is orders of magnitude higher than the 1P system, its amenity to continuous, relatively low-powered NIR sources is a significant advantage over the 2P and SHG systems.

3.1. Upconversion Nanoparticles

UCNPs are phosphorescent crystalline nanomaterials which act as NIR-powered lightbulbs, absorbing NIR photons and converting them to UV/vis photons. In each upconversion event, multiple low-energy photons are absorbed to furnish relatively long-lived (up to several milliseconds^[49]) real excited electronic

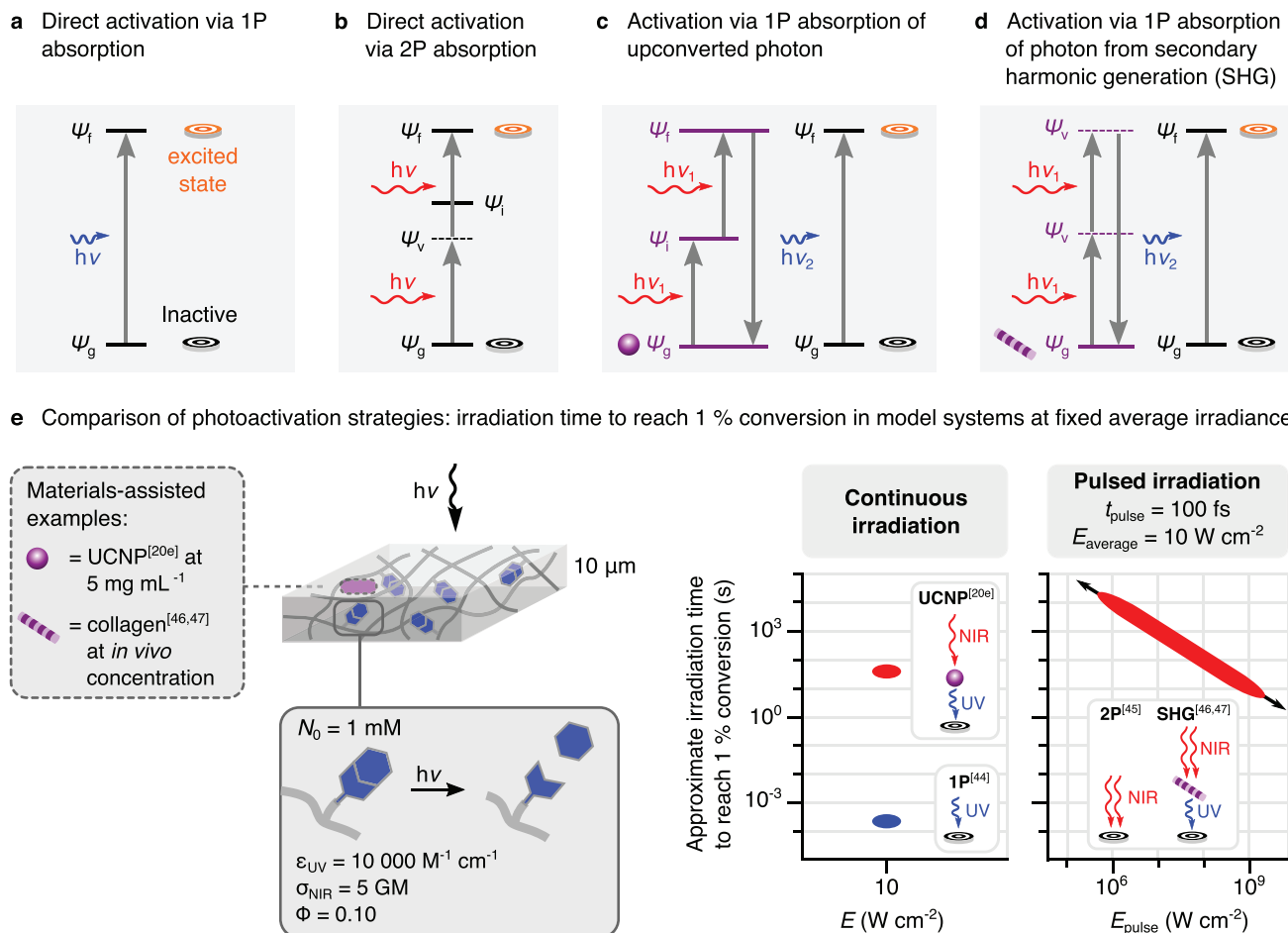


Figure 3. Strategies for direct path photoactivation of in vivo targets through tissue. a–d) Simplified energy level diagrams for the four direct path photoactivation strategies, with simplified energy levels for the photoactivatable target shown in black, and simplified energy levels for transducing materials shown in magenta. Symbols: ψ_g = ground state, ψ_f = final real excited state, ψ_v = virtual excited state, ψ_i = intermediate real excited state, h = Planck's constant, ν = photon frequency. e) Comparison of the four excitation strategies using exemplary photophysical properties for common 1P ($\epsilon_{UV} = 10^4 \text{ L mol}^{-1} \text{ cm}^{-1}$) and 2P ($\delta_{NIR} = 5 \times 10^{-50} \text{ cm}^4 \text{ s photon}^{-1} \text{ molecule}^{-1} = 5 \text{ GM}$) photoremovable protecting groups (PPGs) used for bioactive molecules and assuming a photolysis quantum yield $\Phi = 0.1$. The average irradiance is held constant at 10 W cm^{-2} across the four scenarios, with the impact of increasing pulse irradiances (and therefore decreasing repetition rate) shown for the 2P and SHG activations. The 1P-activated photocleavage is at the low concentration limit (absorbance < 0.02) giving a first order rate equation used to determine the irradiation time.^[44] Derivation of the 2P-activated photocleavage rate was emulated from Klan and co-workers.^[45] Material-assisted scenarios were derived from the reported photocleavage rates for a similar hydrogel photoactivation by Zheng et al.^[20e] using NaYF₄:TmYb particles at 5 mg mL^{-1} and the SHG efficiency values determined by Hochheimer et al.^[46] and Guo et al.^[47] for collagen-rich tissue. Note that in the SHG scenario, the contribution of 2P activation is omitted to show only the effect of SHG photons.

states, which can revert to the ground state by emission of a single high-energy photon.^[30] Typically, crystalline host matrix of NaYF₄ is doped with i) sensitizer ions (e.g., Yb³⁺), responsible for efficient NIR absorption, which transfer energy to ii) activator ions (e.g., Er³⁺ or Tm³⁺) responsible for emission. The emission spectrum of the UCNPs can be tuned to particular wavelengths by controlled lanthanide doping.^[50] The brightness B_{UC} is defined as:

$$B_{UC} = \sigma(\lambda_{ex}) \Phi_{UC}(E) \quad (2)$$

where $\sigma(\lambda_{ex})$ is the absorption cross section at excitation wavelength λ_{ex} , and $\Phi_{UC}(E)$ is the quantum yield of upconversion

(i.e., number of emitted photons divided by number of absorbed photons), also referred to as the luminescence efficiency, at incident irradiance E .^[30] Upconversion quantum yield increases with irradiance E until saturation effects dominate above $\approx 100 \text{ W cm}^{-2}$.^[51] Upconversion is orders of magnitude more efficient than 2P processes at low irradiances, and low powered continuous-wave (CW) diode lasers are sufficient to drive meaningful UCNP emission.^[52] Nonetheless, absorption cross sections are modest, and luminescence quantum yields at biologically-relevant irradiances are typically < 0.01 . More efficient UCNPs that can deliver a given UV or vis emission intensity at lower excitation power are therefore continuously sought. Increasing UCNP brightness, shifting the absorbance

maximum to the most tissue-transparent part of the NIR spectrum, reducing the distance between UCNP and photoactivatable target through targeting, and improving biocompatibility^[53] have all been central to improve the effectiveness of UCNP in biomedical scenarios. While comprehensive details on UCNP development can be found elsewhere,^[30] key features for in vivo light delivery are outlined here.

3.1.1. Maximizing Luminescence Efficiency of UCNPs

Extensive work has been done in the last decade to increase UCNP luminescence efficiency. One of the main approaches is minimizing surface quenching effects by installing a passivating shell which increases the quantum yield of luminescence.^[30] The shell can be crystalline inorganic matrix similar to the core, for example, NaYF₄,^[54] or NaGdF₄,^[55] or an amorphous layer, for example, SiO₂,^[56] and prevents quenching of the sensitizer excited state with surrounding molecules. The ability to produce controlled core-shell structures was a significant advance in the field, and has been recently extended to produce even more sophisticated designs. Wang and co-workers synthesized core-shell-shell UCNP in which the doped layer was confined between inert core and outer shell of NaYF₄.^[57] This confinement reduced long-distance quenching between Yb ions, and gave a threefold increase in upconversion emission at ~550 nm versus core-shell particles in which the entire core was doped. The concentration of dopant ions also significantly impacts the efficiency. Prasad and co-workers for example showed that increasing the Yb content from 30 to 99.5 mol% in the shell increased luminescence efficiency sixfold.^[58]

3.1.2. Shifting UCNP Absorbance to More Tissue-Transparent Wavelengths

Excitation of Yb³⁺ sensitizer occurs at 980 nm, but water also exhibits a local absorption maximum at this wavelength which causes heating.^[59] Shifting the absorbance of UCNP to ~800 nm reduces this unwanted heating, and has been achieved by installing either i) organic dyes, for example, IR-806, on the UCNP surface in direct contact with the sensitizer layer (Yb³⁺),^[60] or ii) Nd³⁺ ions in a sensitizer-containing shell layer.^[61] These co-sensitizers absorb at ~800 nm and transfer energy to the Yb³⁺ sensitizer to continue the upconversion cascade. The benefits of such particles have been demonstrated in vitro and in vivo. Han and co-workers used poly(methyl methacrylate) (PMMA) surfaces containing dye-sensitized UCNP to stimulate the firing of 2D-cultured neurons.^[62] The broadband absorbance, and higher absorption coefficient meant that exciting the dye-bearing UCNP at 800 nm gave a sevenfold higher absorbance than dye-free particles at 980 nm. Limited photostability of the dyes, complicated functionalization, and hydrophobicity are disadvantages of organic dyes, and the need to spatially isolate the Nd³⁺ in sophisticated (multi)core-shell structures is demanding.^[30] Shifting the absorbance to ~800 nm has been a breakthrough for biomedical potential of UCNP.

Although UCNP with NaYF₄ at their surface cause rapid cell mortality,^[63] the installation of an inert shell of silica renders particles biocompatible on a month timescale.^[21] UCNP in deep mouse brain tissue in fact show very little diffusion, permitting successful optogenetic stimulation weeks after injection.^[21] Other shell coatings have been used to provide in vivo biocompatibility and hydrophilicity to UCNP, including phospholipids^[58] and poly(acrylic acid).^[21] Even with such functions, longer term biocompatibility and clearance studies are required before free UCNP reach the clinic.

3.2. Second Harmonic Generation Materials

SHG is a coherent, non-linear light scattering process in which two incident photons interact almost simultaneously with a non-centrosymmetric material to form a single photon with exactly twice the energy (Figure 3d).^[64] SHG is most pronounced from materials that exhibit high organization and orientation, which includes endogenous structural protein arrays of collagen^[65] and to a lesser extent microtubules^[66] and actomyosin.^[67] SHG-based imaging of these species is well established in vitro and progressing in vivo,^[68] opening up intriguing options for using SHG to perform in vivo photochemistry. Barhoumi et al.^[69] reported the release of a UV-activatable fluorescent dye covalently bound to native collagen fibers in the stroma of rabbit cornea by irradiation with a CW NIR laser (730 nm, 3.8 W cm⁻², 2 h), with the modest fluorescence increase attributed to SHG-mediated photocleavage. Since SHG signal scales with the square of the irradiance, it is remarkable that SHG-induced decaging could be achieved using such a CW laser,^[69] with femtosecond pulsed lasers with irradiances at least in the MW cm⁻² range typically required for meaningful SHG outputs that could drive photochemical reactions. The efficiency of SHG is defined as the number of scattered photons with double frequency divided by the number of incident photons. Efficiency was measured at 6×10^{-9} in the collagen-rich rabbit cornea^[46] at $E_{\text{pulse}} = 1 \text{ MW cm}^{-2}$. Moving to the GW cm⁻² pulse regime predictably gives SHG efficiencies ~10³-fold higher.^[47] Very short, high irradiance pulses would therefore be preferable for maximizing SHG efficiency for in vivo photochemistry. Endogenous materials such as metal or metal oxide nanocrystals with non-centrosymmetric crystal structures^[70] have also demonstrated SHG efficiencies 1 to 2 orders of magnitude higher than native proteins,^[71] and could be exploited as SHG transducers for in vivo photoreactions. Bismuth ferrate (BiFeO₃, BFO) and lithium niobate (LiNbO₃, NLO) are particular standouts that show high SHG efficiency^[72] and low cytotoxicity.^[73] Demonstrations of L-tryptophan and anticancer drug chlorambucin release from LNO particles by cleavage of curcumin linkers have provided a glimpse of in vivo potential,^[74] but the in vitro irradiation conditions of $E_{\text{pulse}} = 300 \text{ GW cm}^{-2}$ (790 nm, 50 fs pulses, 1 kHz repetition rate, $E_{\text{average}} = 15 \text{ W cm}^{-2}$) required 25 min for 80% release, with a significant proportion of this release occurring through 2P activation despite the photocleavable groups not being optimized for 2P absorption.^[74b] An SHG-driven model photoreaction therefore proceeds with comparable efficiency to a 2P photoactivation, as illustrated in Figure 3e, and is accompanied by the same hardware requirements (pulsed laser,

complicated optics) that hamper in vivo adoption. UCNP can efficiently convert long wavelength photons to short wavelength ones at much lower irradiances, but the lossless nature of SHG accompanied by its wavelength independence may encourage further developments in vivo especially as more efficient, cyto-compatible “harmophores” are developed.

3.3. Application Scenarios Demonstrating Direct Path Excitation

Optogenetic treatments, light-triggered drug delivery systems, and light-based manipulation of implanted materials for regenerative medicine are pre-clinical scenarios in which direct path photoactivation approaches have been developed. The treatment of cancers using PDT is an established clinical approach that has also benefitted from recent innovations in light management, and may be the first to apply these new light delivery approaches clinically. We briefly outline the status of each category, and highlight how innovations in light delivery are combating limited light penetration depths and broadening the scope of each technique.

3.3.1. Optogenetics

The most recognized and burgeoning branch of optogenetics uses genetic engineering to introduce light-responsive ion channels into electrically active cells like neurons. The light-active molecules are typically opsins, that is, photoactive ion channel proteins from light-responsive algae, that allow control of ion transport through the membrane using vis light.^[75] Since its origins in brain research, optogenetics has been extended to electrically-active cells in the spinal cord, heart, and muscles.^[76] Beyond this flagship domain, the optogenetics field encompasses any cell in which gene transcription or the function of transcribed proteins can be manipulated by light, and therefore includes cell-based drug and biopolymer factories and cell-based sensors. We address light management strategies for neuronal and non-neuronal optogenetics separately in this section, since irradiance requirements are distinctly different.

Inducing or inhibiting action potentials in neuronal optogenetics involves the isomerization of opsins in the cell membrane, typically requiring millisecond-scale pulses of blue or green light at $>100 \text{ mW cm}^{-2}$.^[76] A typical neuronal optogenetic experiment might involve delivery of 5 ms pulses of 473 nm light at 20 Hz for 1 s, and observing localized neuron network activation or organism-level behavioral effects. The strong attenuation of 473 nm light by tissue means that honoring the $E_{\text{max}}(5 \text{ ms}) = 11 \text{ W cm}^{-2}$ (Figure 2c) would mean that sufficient irradiance for opsin activation ($>100 \text{ mW cm}^{-2}$) could only be achieved down to a depth of $\approx 2 \text{ mm}$ (Figure 2b), which is barely sufficient to reach the brain through scalp and skull even in small animals. Red-shifted opsins like red-activatable channelrhodopsin (ReaChR)^[77] and ChrimsonR^[78] have been developed more recently to allow activation using longer wavelengths, and therefore benefit from higher penetration depths. Some relatively rare reports have also demonstrated 2P excitation approaches to activate opsins in vivo

with cell-level resolution using NIR photons,^[43,79] but were still only demonstrated at depths of $<1 \text{ mm}$ in brain tissue that was exposed by inserting a transparent window through the scalp, skull, and dura mater.^[43]

UCNPs have made an important contribution to neuronal optogenetics by allowing excitation of vis responsive opsins using NIR wavelengths. The UCNP can be directly injected into the desired brain region, or housed in an implantable device. An important paper by Chen et al. used UCNP for deep brain stimulation in live mice with skin and skull intact (Figure 4a).^[21] This work quantified the relationship between NIR excitation irradiance, tissue heating, and UCNP emission intensity in deep tissue, providing realistic bounds for UCNP utility in vivo. Pulses of NIR light (2 W laser, 980 nm, 15 ms pulses) projected at 140 W cm^{-2} on the skull surface ($E/E_{\text{max}}(15 \text{ ms}) = 1.5$, Point C in Figure 2c) achieved $\approx 1 \text{ W cm}^{-2}$ at a depth of 4.5 mm in mouse brain, and generated 6.3 mW cm^{-2} of upconverted blue light from 0.18 mg of UCNP injected at that location. Such modest emission intensities successfully generated photocurrents in co-located neurons to control animal behavior, but were accompanied by rapid temperature rise at the brain surface. Delivery of pulses at 20 Hz for just 3 s ($E_{\text{average}}/E_{\text{max}}(3 \text{ s}) = 24$, Point D in Figure 2c) raised the brain tissue surface temperature by $>15^\circ \text{C}$. Although this irradiation profile was shown to be non-cytotoxic, attenuation and associated heating effects of 980 nm light were clearly significant. Improving brightness (absorption cross section and/or quantum yield) and shifting the absorption maximum to a more penetrating wavelength $\approx 800 \text{ nm}$ (Section 3.1.2) could further increase the depth at which UCNP-mediated optogenetics could be applied in the deep brain.

Rather than injected UCNP, implanted devices containing UCNP have also been used for direct path optogenetics, preventing interaction of UCNP with tissue and potential diffusion-based dilution. The first example of UCNP-based neuronal optogenetics in live rodents encapsulated UCNP in hollow glass microneedles $<100 \mu\text{m}$ in diameter and weighing $<1 \text{ mg}$ (Figure 4b).^[40] which demonstrated long-term (6 month) biocompatibility despite inducing some mild inflammation due to the high stiffness of glass. The diameter and weight of the device were more than an order of magnitude lower than the smallest implantable light-emitting diode (LED) systems. The tight packing and permanent confinement of UCNP in the microneedle tip allowed the stimulation of deep neurons (Figure 4c) at remarkably low NIR irradiances (980 nm, 500 mW cm^{-2} , 10 ms pulses at 20 Hz over 500 ms) that were far below the MPE for human skin, with $E/E_{\text{max}}(10 \text{ ms}) = 0.004$ and $E_{\text{average}}/E_{\text{max}}(500 \text{ ms}) = 0.01$ (Figure 2c, Points E and F). Light delivery was aided by the significant waveguiding role of the microneedle, which provided a clear path through skull, dura mater, and brain tissue to the device tip. A custom tracking set-up was used to provide remote NIR irradiation to the head of freely-moving mice. Similar work from the same group used more efficient core-shell-shell UCNP for in vivo neuron inhibition in behaving mice,^[57] which requires much higher optical power than excitation experiments and was therefore a worthy target of more efficient particles. At an irradiance of 600 mW cm^{-2} the core-shell-shell device induced complete neural inhibition (Figure 4d) while a comparable core-shell device triggered neural inhibition only sporadically, highlighting

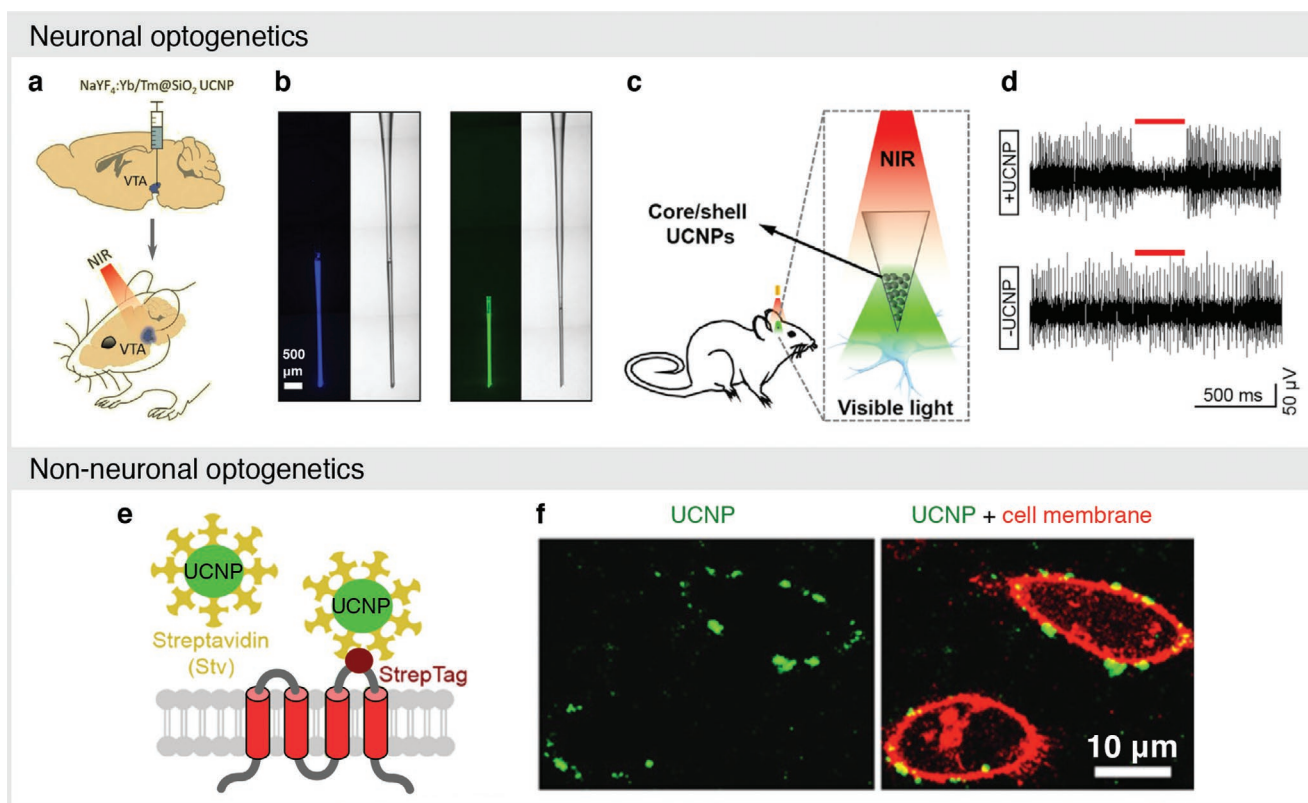


Figure 4. Direct path light-management strategies for optogenetics, drug delivery, hydrogel formation and photomanipulation, and PDT. a) UCNP-mediated optogenetics for deep transcranial brain stimulation using NIR light. Adapted with permission.^[21] Copyright 2018, The American Association for the Advancement of Science. b) Bright-field and fluorescence images of implantable micro-needles containing UCNP doped with Tm^{3+} (blue) or Er^{3+} (green). Implanted devices were used for c) optogenetic control of brain activity and animal behavior in free-moving mice by shining external NIR light on the head. Reproduced with permission.^[40] Copyright 2017, Elsevier. d) In vivo neural recordings using a similar implanted device showed optogenetic inhibition of engineered neurons in response to low-irradiance NIR light (980 nm, 600 mW cm^{-2}). Reproduced with permission.^[57] Copyright 2018, American Chemical Society. e) UCNP-coated streptavidin could target a streptavidin-binding tag (StrepTag) introduced into light-responsive ion channel proteins. f) Fluorescence microscopy showed anchoring of the UCNP (green) at the cell membrane (red), later facilitating non-neuronal optogenetic therapy using NIR light. Adapted with permission.^[80] Copyright 2015, eLife Sciences Publications.

the importance of the enhanced upconversion efficiency. The temperature increase in brain tissue was $<0.5^\circ\text{C}$ using a similar pulse regime delivered over a 5 min period. A null device devoid of UCNP and irradiated with 532 nm green laser (50 ms pulse width, 1 W cm^{-2}) showed no neural inhibition, highlighting the importance of the UCNP for the success of the system. UCNP therefore offer promising opportunities to shift the excitation wavelength for optogenetics into the NIR region using relatively low powered lasers.

Non-neuronal optogenetics involves controlling gene expression or protein localization/function in non-neuronal cells using light, and typically uses irradiation periods of seconds to minutes delivered regularly over hours to days to elicit longer-acting biological changes. As a representative in vivo example,^[22] subcutaneously injected cells engineered to express glucose-controlling proteins under blue light exposure (470 nm LED, 5 s ON/10 s OFF, 0.64 mW cm^{-2} , $E/E_{\text{max}} = 0.003$) could effectively control blood glucose levels in a diabetic mouse model, which is remarkable given the low irradiance value. 2P excitation has also been demonstrated for in vivo non-neuronal optogenetics, for example, to optically control the migration, adhesion, and chemokine secretion of single engineered T-cells

introduced into mouse lymph nodes,^[81] but in this case involved surgically exposing the lymph node. Materials-assisted light delivery is more prevalent and practical. In a ground-breaking report, Zhou and co-workers used UCNP for efficient excitation of optogenetically engineered immune cells by blue light upon remote NIR irradiation.^[80] In a mouse melanoma model, 980 nm light delivered from day 3 to day 9 (8 h per day, 1 min ON/1 min OFF, 3 W cm^{-2} , $E/E_{\text{max}} = 4.1$) triggered Ca^{2+} influx in the optogenetically-modified immune cells, which upregulated the mouse immune response and more than halved the tumor growth by day 18. The UCNP were specifically functionalized to facilitate membrane binding (Figure 4e,f), which has been demonstrated to facilitate colocalization of UCNP with their light-responsive target and thereby minimize the light dose for optogenetic stimulation.^[58,80,82]

3.3.2. Phototriggered Drug Release

The controlled manipulation of a therapeutic species is a highly appealing domain of in vivo light delivery, and falls into two broad approaches. The first approach incorporates

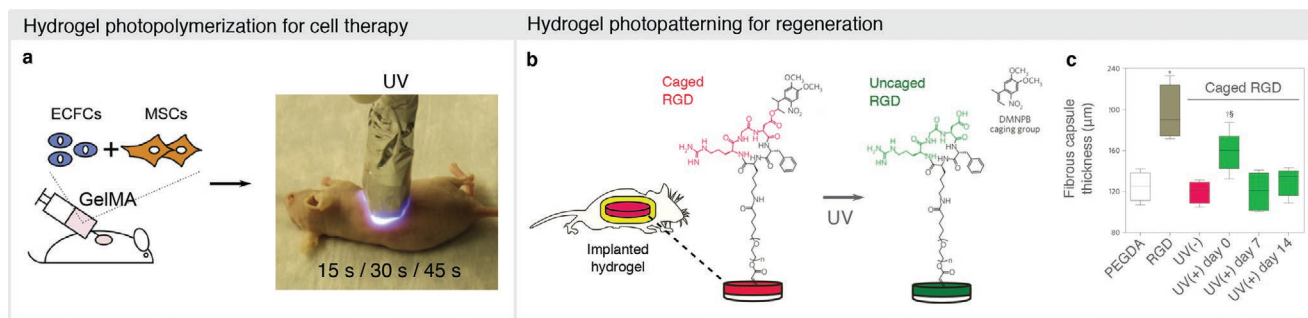


Figure 5. Direct path light-management strategies for hydrogel formation and photomanipulation. a) Vascular network bioengineering by photocuring a subcutaneously-injected gelatin methacrylate (GelMA) solution containing human endothelial colony-forming cells (ECFCs) and mesenchymal stem cells (MSCs) using UV light (40 mW cm^{-2} , 15–45 s). Adapted with permission.^[90] Copyright 2013, Elsevier. b) Subcutaneously implanted hydrogels bearing caged cell-adhesive ligand RGD could be activated using transdermal UV light at defined timepoints. c) Delayed photoactivation (day 7, day 14) significantly reduced fibrous encapsulation of the implant versus immediate decaging (day 0). ANOVA ($n = 4\text{--}6$) $\S p < 0.05$. Adapted with permission.^[5] Copyright 2014, Nature Publishing Group.

light-responsive functionality into the molecular structure of the therapeutic itself (photopharmacology), allowing administration of the inactive form followed by subsequent photoactivation by inducing conformational change (photoswitching) or irreversible cleavage of a photoremovable protecting group (PPG).^[8] Application of such photopharmacology systems in vivo has largely progressed hand in hand with the development of long-wavelength photoswitches and PPGs, with some 1P photoactivations permitted using red or even NIR photons.^[83] The scope for materials-assisted light delivery in these systems, however, is limited due to their molecular nature.

The second approach for phototriggered drug delivery relies on a photoresponsive delivery depot (e.g., implant, microparticle, nanoparticle, or cell) that can release a loaded therapeutic through light-driven linker cleavage, polarity switching, or confinement change in the carrier material.^[84] Materials that assist in the light delivery process or more efficiently utilize delivered photons have been integrated into many of these platforms. UCNPs coated with mesoporous silica, for example, have released hydrophobic drugs in vivo upon NIR irradiation.^[23] A hydrophobic spiropyran coating on the silica surface supported entrapment of the hydrophobic drug curcumin in the dark state, while NIR irradiation (980 nm, 3 W cm^{-2} , 20 min, $E/E_{\text{max}}(20 \text{ min}) = 4.1$) produced UV that isomerized spiropyran to its hydrophilic state and triggered curcumin release. Similar particles were used to suppress tumor growth in live mice by photocleaving a protective poly(ethylene glycol) (PEG) layer to release physically-entrapped siRNAs for cancer gene knock-down.^[24] Other UCNP-based release systems, for example, a cancer therapy platform that used upconverted UV/vis photons to drive the in situ reduction of Pt(IV) pro-drug to highly cytotoxic Pt(II),^[85] a platform to photocontrol intracellular calcium levels for stem cell differentiation,^[86] and light-triggered systems for remote gene editing,^[87] may also become clinically relevant.

3.3.3. Polymerization, Bioactivation, or Degradation of Hydrogels for Cell Therapies and Tissue Regeneration

Cell therapies and regenerative materials rely on injectable materials that can encapsulate cells and support and guide their

function at the damaged site, with light offering possibilities to initiate crosslinking for cell encapsulation, activate biochemical effectors that control cellular processes, and/or degrade the crosslinked network on command. We focus on key advances from the light delivery perspective in vivo, and readers are directed to the recent reviews by Lindberg et al.^[88] (in vivo photopolymerization) and Zhu et al.^[89] (photopatterning/photodegradation of hydrogels) for broader overviews.

In vivo photopolymerization of hydrogels for tissue engineering and cell therapy initially used traditional UV-responsive photoinitiators and acrylate-based precursors, but the limited penetration depths would make them difficult to translate to humans. For example, a GelMA hydrogel containing human endothelial and stem cells was implanted transdermally in nude mice (Figure 5a) and polymerized using a safe UV light dose (40 mW cm^{-2} , 15 s, $E/E_{\text{max}} = 0.6$).^[90] Regeneration of vascularized tissue was demonstrated, but higher UV doses compromised microvessel formation. Translation to humans would require significantly higher UV irradiances due to approximately tenfold greater skin thickness (1–2 mm on average^[91]). Elisseff for example used human skin mimics to study the transdermal photopolymerization at UV and vis wavelengths for their murine cartilage regeneration system, providing more clinically-relevant insights.^[92] UV exposure achieved only 80% conversion after extended irradiation (360 nm , 100 mW cm^{-2} , 900 s, $E/E_{\text{max}} = 90$) using the UV-responsive photoinitiator Irgacure 184. Switching to vis light achieved the same conversion much more rapidly at safe irradiance (550 nm , 100 mW cm^{-2} , 100 s, $E/E_{\text{max}} = 0.6$) due to the higher transmittance of 550 nm photons (which compensated for the low absorbance of the initiator in the vis range). Eosin Y ($\lambda_{\text{max}} \approx 525 \text{ nm}$) has been used to initiate transdermal curing of an acrylated PEG/hyaluronic acid-based hydrogel in the vis range (520 nm , 43 mW cm^{-2} , 2 min, $E/E_{\text{max}} = 0.22$) for reconstruction of soft tissue in humans to a depth of 5 mm.^[33] More recently, a cobalt complex based on vitamin B₁₂ demonstrated more efficient radical generation under 660 nm irradiation than Eosin Y at 520 nm, perhaps permitting even deeper in vivo photocuring by avoiding absorption by melanin and hemoglobin.^[15] On the materials front, UCNPs have yet to transition from in vitro demonstrations^[93] to in vivo ones, with avoidance

of excessive heating from abundant NIR photons likely to be a key consideration. Radical polymerization is intrinsically exothermic, and the combined heating effects from the light source, the absorbed photons, and the radical polymerization process need to be in scope when developing new systems. Thiol-ene based photopolymerizations, which link thiol- and vinyl-bearing precursors through a step-growth mechanism,^[94] are receiving surging interest in the biomaterials community because polymerization can be performed at lower light doses than in acrylate systems.^[95] Thiol-ene crosslinking could complement developments from the light delivery perspective (e.g., UCNPs) for building deeper in vivo regenerative materials without excessive heating.

Photopatterning and photodegradation are powerful tools for dynamically controlling the properties of photoresponsive hydrogels, thereby providing signals to embedded cells. The activation of phototriggerable bioactive ligands (i.e., cell adhesive molecules or growth factors enclosed or bonded to the hydrogel matrix after implantation) can support cellular development and therapeutic function by providing instructive signals to the cells at selected time points and locations. Lee et al. demonstrated that light-exposure of PEG diacrylate (PEGDA) hydrogels functionalized with a UV-photoactivatable cell adhesive ligand (Figure 5b) could spatially control vascularization and reduce the fibrotic response to the material implanted subcutaneously (depth $\approx 150\ \mu\text{m}$) in mice, highlighting the benefit of delayed post-operative photoactivation (Figure 5c).^[5] Despite no observed photodamage from the UV exposure (351 nm, $20\ \text{mW cm}^{-2}$, 10 min), the dose exceeded safe levels ($E/E_{\text{max}} = 12$, Figure 2c, Point B) that would again hinder translation to humans. The incorporation of UCNPs (0.5% w/v) into hydrogels functionalized with the same UV-responsive bioactive ligands recently allowed activation through 2.5 mm of ex vivo porcine tissue using a high dose of NIR light (974 nm, $15\ \text{W cm}^{-2}$, 40 min, $E/E_{\text{max}} = 20$).^[20e] The successful photocleavage triggering embedded endothelial cells to form microvasculature networks over the next 24 h, and demonstrates the benefit of UCNPs for materials-assisted light delivery. Active cooling was nonetheless required to compensate for the significant heating effect, highlighting that more efficient UCNPs (such as those responsive to $\approx 800\ \text{nm}$ light) are needed to bring NIR exposures to safe levels and/or access deeper structures in vivo. 2P excitation has also been demonstrated as a niche light delivery method for long-wavelength photopatterning of hydrogels and tissues using a photoactivated click reaction,^[96] with 3D patterning at micron-scale resolution demonstrated to a depth of hundreds of microns. The photoactivation at 690 nm was achieved with individual pulses below safe levels (140 fs pulses, $E = 2.7 \times 10^9\ \text{W cm}^{-2}$, $E/E_{\text{max}}(140\ \text{fs}) = 0.02$) and average irradiance just above safe levels (pulses delivered at 1 kHz for 1 h, $E_{\text{average}} = 0.373\ \text{W cm}^{-2}$, $E_{\text{average}}/E_{\text{max}}(1\ \text{h}) = 1.9$). Precise patterning/labeling of in vivo tissue or implanted biomaterials could be envisaged for some specialized scenarios, but would probably require a transparent window similar to 2P-activated optogenetics systems.^[43] Finally, degradation of in vivo hydrogels has been achieved using implanted hydrogel matrices containing photodegradable groups.^[97] Photodegradable hydrogels containing o-NB linkers were used to temporarily seal bariatric balloons (i.e., devices which control satiety) in pigs, and UV light

(365 nm, $11.8\ \text{mW cm}^{-2}$, 30 min) was delivered endoscopically to degrade the seal and trigger deflation.

While these reports demonstrate proof-of-concept applications for photoresponsive hydrogels in vivo, we see the most potential for light-modulable hydrogels residing in deeper tissue applications beyond sub-dermal regions and endoscopically-accessible cavities. Coupling the material-assisted light delivery strategies described in this review to these photoresponsive systems will open up exciting new possibilities for deep-tissue regeneration.

3.3.4. Photodynamic Therapy

PDT is a clinically-applied cancer therapy facilitated by a systemically or topically administered photosensitizer (PS) species.^[98] After light absorption, the PS undergoes intersystem crossing to generate a triplet excited state which transfers energy to molecular oxygen, generating highly cytotoxic singlet oxygen and ROS that directly kill nearby cancer cells.^[99] PDT is also emerging as a treatment for bacterial infections.^[100] Clinically employed PS species are generally porphyrin or chlorin derivatives with main absorbance band at $\approx 400\ \text{nm}$ and weaker absorbances at 600–700 nm.^[101] Inorganic PS species responsive to UV, such as TiO_2 nanoparticles, are also used.^[102] For clinical light delivery, non-invasive, direct irradiation of tumor tissue using diode lasers or LEDs is restricted to superficial tumors, with endoscopy and/or surgical access required for deeper tumors or internal surfaces such as lung or prostate tumors. Optical fibers incorporating side-emission zones or lenses have been the leading clinical technology utilized for spatially precise dispersion of light inside deep tumors^[101] (Section 4.3.2).

The irradiation regime for clinical PDT varies by tumor type and PS, but as a guideline,^[101] continuous or pulsed light with moderate irradiance of $5\text{--}250\ \text{mW cm}^{-2}$ is typically delivered to the tumor for minutes up to an hour, corresponding to radiant exposures of $20\text{--}200\ \text{J cm}^{-2}$, which is sometimes repeated within a week or month timescale. Lower irradiances and light fractionation regimes (e.g., 1 min ON/1 min OFF) can be orders of magnitude more effective than shorter, continuous durations of higher irradiance light^[103] by avoiding oxygen depletion.^[104]

Despite proven benefits, PDT is not the front-line oncological intervention in part due to the challenge in providing appropriate light doses. UCNPs offer significant benefit in PDT by facilitating non-radiative energy transfer of absorbed NIR photons to a PS species usually bound to the particle surface. The 660 nm red emission of $\text{NaYF}_4\text{:Yb,Er}/\text{NaGdF}_4$ core-shell UCNPs, for example, overlaps with the absorption peak of PS chlorin e6 to facilitate singlet oxygen generation. When injected intravenously in mice, accumulation in tumors allowed direct path irradiation with NIR at the tumor site (980 nm, $600\ \text{mW cm}^{-2}$, 5 s ON/10 s OFF for 5 min, $E/E_{\text{max}} = 0.8$) to halt tumor growth while control tumors increased eightfold in volume over the 2 week period.^[105] Other reports have incorporated several PS species in the same platform to harness the multiple wavelengths emitted by the UCNPs.^[106] Advances in UCNP fabrication that shift the absorption wavelength to $\approx 800\ \text{nm}$, optimize the emission profile toward particular PS species, and improve the brightness have all been utilized in recent UCNP-driven

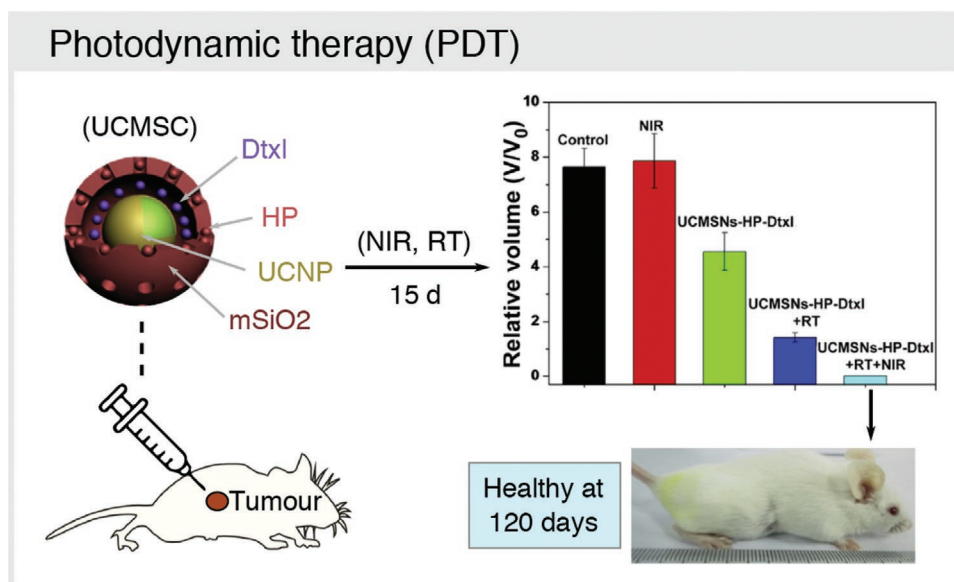


Figure 6. Synergistic PDT combining UCNP photosensitization of hematoporphyrin (HP) using NIR light (980 nm, 2.5 W cm⁻², 1 min ON/1 min OFF for 30 min) with delivery of doxorubicin (Dtxl) and radiotherapy (RT) to eradicate tumors by day 15. Animals remained tumor-free up to 120 days. Adapted with permission.^[110] Copyright 2014, Elsevier.

PDT systems.^[25] The incorporation of additional functionalities into the UCNPs, particularly tumor-targeting groups,^[107] chemotherapy drugs,^[108] and oxygen replenishing species,^[109] have further augmented PDT efficacy^[25] and show the most promise for clinical translation. Bu and co-workers, for example, loaded a mesoporous silica shell of UCNPs with PS and the chemotherapeutic Dtxl.^[110] NIR-driven PDT (980 nm, 2.5 W cm⁻², 1 min ON/1 min OFF for 30 min, $E/E_{\max}(1 \text{ min}) = 3.4$) combined with both chemo- and radiotherapy completely eliminated tumors in mice (Figure 6), highlighting how additional anti-tumor functions of UCNPs can complement the light-driven PDT for improved treatment outcomes.

3.4. Conclusions and Outlook for Direct Path Light Delivery

The direct delivery of light through tissue, where feasible, offers the least invasive photoactivation strategy for a range of in vivo processes. The scattering and absorption of light by tissue are most prominent at shorter wavelengths, which restricts activation using UV and short vis to shallow targets down to just a few hundred microns below the skin surface (Figure 2b). Accessible targets include photoresponsive drugs administered to superficial cancers, or subcutaneously implanted biomaterials and drug delivery systems. Using higher incident irradiances to deliver more photons to a particular depth is constrained by the MPE on skin, which is particularly stringent for UV wavelengths. Penetration depth improves with increasing wavelength, increasing from hundreds of microns for blue light to several centimeters in the first NIR window (700–900 nm). An increasing MPE with increasing wavelength provides further incentive to exploit this spectral region, but photoresponsive groups that can be directly activated using the less energetic NIR photons are relatively scarce despite growing efforts to

expand the available range. Those which have been successfully employed in vivo have been highlighted above.

Strategies for accumulating the energy of multiple NIR photons offer more fertile ground for direct path photoactivation at substantial tissue depths up to several centimeters. Seeking photoresponsive groups that exhibit significant 2P absorption cross sections throws the developmental challenge to the synthetic chemist, much like the development of 1P photoresponsive groups activatable by NIR. The drawbacks of 2P-responsive groups are usually significant: synthetic complexity and often low water solubility of extended conjugated systems, accompanied by the need for delivering very high photon fluxes into very small focal volumes for photoactivation, which can only be achieved with expensive and clinically cumbersome femtosecond pulsed lasers. Developing targets responsive to 2P absorption is therefore the most restrictive of the direct activation approaches for pooling the energy from multiple NIR photons.

More promising are the materials-assisted strategies of i) UCNPs, and ii) non-centrosymmetric materials with high SHG capacity. UCNPs act as in situ light transducers by absorbing NIR photons and emitting UV or vis photons. The in situ generation of high energy photons from low energy ones takes advantage of the higher NIR penetration depth, and only exposes tissue in the immediate vicinity of the UCNPs to more energetic photons. The long lifetimes of the intermediate excited states also allow upconversion to be driven by low-powered, low-cost light sources, which is a significant advantage for clinical implementation. The utility of UCNPs has been demonstrated across most of the applications for which direct light delivery is desired (Figure 1c–f), ranging from minimally invasive optogenetics in the deep brain to injectable drug delivery platforms. Their translation to the clinic will rely on comprehensive proof of biocompatibility, which is still ongoing.

Tailoring of the surface properties of systemically-administered UCNPs to enhance binding/accumulation in specific tissue of interest and ensure appropriate clearance pathways post-administration will be key milestones. Innovations in controlling nanoscale structure and composition continue to improve absorption efficiencies and luminescence quantum yields to minimize unwanted tissue heating and maximize penetration depth. The potential of UCNPs extends beyond their use as free particles to implantable composite materials, which offer the benefits of upconversion while restricting the particles within the device. Confinement to a device may fast-track clinical approval by avoiding direct interaction with the body. Appropriate degradation, clearance, or removal of such platforms will still be required to complete their life cycle with minimal patient impact.

Another less common approach for pooling the energy of multiple NIR photons to produce a higher energy photon is SHG, which can be considered the scattering equivalent of 2P absorption. The implication here is that the two NIR photons need to interact almost simultaneously with the SHG (non-centrosymmetric) material, again requiring high powered pulsed lasers to achieve meaningful SHG efficiencies. The ability of the abundant structural protein collagen to undergo SHG is appealing for its employment *in vivo* without needing an endogenous material. While exploited extensively for 2P imaging of collagen, the effect has only recently been explored for *in vivo* photoactivation in animal eyes. Other SHG-capable materials may offer further options for *in vivo* photoactivations, while acknowledging that exogenous materials bring additional complexity from the invasiveness and biocompatibility standpoints and probably still require high powered NIR sources. If proven safe, we therefore see UCNPs as the more versatile materials for materials-assisted photoactivations using direct path irradiation. The cap on NIR penetration to a maximum depth of a few centimeters, at which point >99% of the delivered photons have been lost en route to the target, nonetheless calls for alternative strategies for more photon-efficient light delivery to greater depths. Optical waveguides are the leading answer to this call.

4. Clearing the Path: Optical Waveguides

A second materials-based strategy for delivering light into the body is to implant an optical waveguide that transmits light to a desired location, while largely circumventing losses due to scattering and absorption of tissue. Providing a “clear path” for light propagation offers ample penetration depth in a biological setting, provided the waveguide material possesses adequate optical properties. In this section we describe waveguide innovations that show promise for *in vivo* applications, and could be transferred to photoregulated biomaterials. We cover the relevant parameters for their design, the established processing technologies for their fabrication, and demonstrated key application scenarios *in vivo*. Significant attention is given to waveguides based on soft polymeric biomaterials, particularly hydrogels, which appear ideal to be integrated with soft photoresponsive (living) materials. The medical uses of biocompatible waveguides have been recently reviewed by others.^[27,111]

4.1. Design and Properties of Waveguides

Optical waveguides are high refractive index (RI) devices which can confine light and transmit it in a longitudinal (*z*) direction. Optical waveguides are most commonly non-planar and present optical fiber (Figure 7a), channel (Figure 7b), rib (Figure 7c), and ridge (Figure 7d) geometries. Alternatively, they can be planar (slab waveguides, Figure 7e). Waveguiding requires that the light-guiding portion of the waveguide be surrounded by a lower RI material. So-called core-cladding designs ensure this by surrounding the higher RI waveguiding portion with a lower RI material. The RI can change abruptly at the boundary between core and cladding, giving step-index waveguides, or change gradually, giving graded-index waveguides. Almost all core-cladding examples in this review are step-index waveguides due to their simpler fabrication. Although discussion of waveguide modes can be found elsewhere,^[112] it is important to state that a waveguide can support a finite number of so-called guided propagation modes for a given wavelength of light, leading to a classification as either a single-mode or multimode waveguide. The dimensions of the core are the main factor determining the allowed number of guided modes. Single-mode fibers have core diameters <10 μm and support just one guided mode (called the fundamental mode) which travels parallel to the fiber axis, has an amplitude maximum at the fiber center, and therefore experiences minimal loss from interaction with the cladding. As core dimensions increase, more guided modes are supported. These undergo more interactions with the cladding, meaning multimode waveguides—encompassing the majority of examples in this review—exhibit higher optical losses than single-mode fibers. The concept of guided propagation modes is particularly relevant to waveguides which exhibit a change in core dimensions along their *z*-axis, for example in tapered waveguides used for side emission where diminishing core dimensions support fewer guided modes resulting in the out-coupling of light.^[113]

Since the purpose of waveguides is to confine light, optical loss is a critical descriptor of waveguide performance. Optical loss or attenuation (*A*) at a particular propagation distance (*z*) is expressed in decibels (dB) based on the power at that position (*P*) compared with the initial power (*P*₀):

$$A = 10 \log_{10}(P/P_0) \quad (3)$$

By rearranging Equation (3), an optical loss of 1 dB corresponds to the output power *P* (in Watts) declining to 10^(-1/10) *P*₀ ≈ 0.79 *P*₀, and an optical loss of 3 dB means *P* has declined to 10^(-3/10) *P*₀ ≈ 0.50 *P*₀. The attenuation coefficient *α* (dB cm⁻¹) is the optical loss per unit length (*L*):

$$\alpha = A/L \quad (4)$$

The propagation length at which *P/P*₀ = 1/*e* (≈0.37), denoted *L*_e, can be a more intuitive representation of optical loss, especially for comparison with penetration depths of light in tissue discussed earlier (see Figure 2b). In this review, we therefore state both the *α* and *L*_e values for describing waveguide performance.

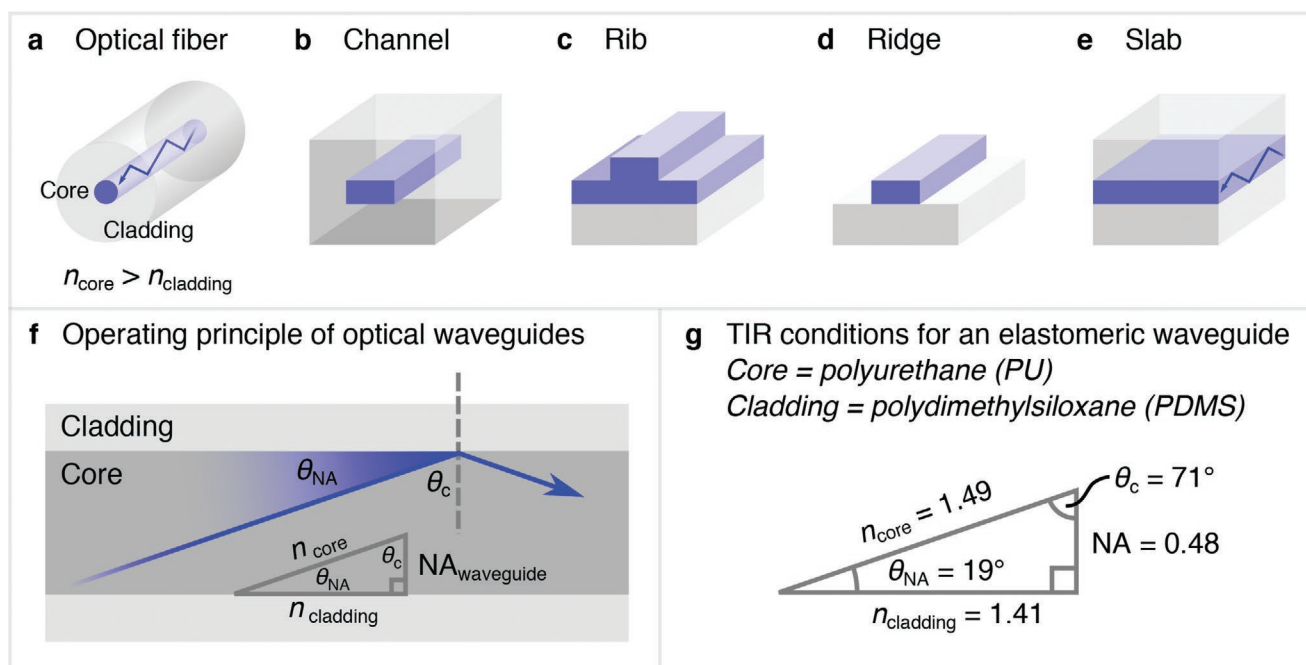


Figure 7. a–e) Waveguide designs. f) Depiction of the range of incident angles (i.e., $\theta < \theta_{NA}$) which can undergo total internal reflection (TIR) in a core–cladding waveguide, showing the geometric relationship between the refractive indices (RIs) of the core (n_{core}) and cladding ($n_{cladding}$) and the numerical aperture (NA), and g) the geometric relationship between these values for the core–cladding waveguide reported by Yun and co-workers.^[114]

The optical loss of a waveguide is defined by the RI (of waveguide and surrounds), optical transparency, and waveguide geometry. The contributions of RI and transparency are described in the next section, followed by a discussion of mechanical properties, which together define the functional performance of a waveguide in a given *in vivo* scenario.

4.1.1. Refractive Index

The first requirement for a waveguide is for the RI of the light-carrying part to exceed that of the surroundings. This permits in-coupled light to undergo total internal reflection (TIR) and thereby remain confined within the waveguide. “Core–cladding” waveguides have the light-carrying portion (core) encased in a lower-RI material (cladding) to facilitate TIR. The RIs of the core (n_{core}) and cladding ($n_{cladding}$) define the numerical aperture (NA):

$$NA = \sqrt{n_{core}^2 - n_{cladding}^2} \quad (5)$$

A larger difference in RI between core and cladding gives a larger NA. Figure 7f shows the geometric relationship in a straight waveguide. A larger NA translates to a larger range of incident angles (relative to the fiber axis) which can undergo TIR. The maximum incident angle which can undergo TIR (θ_{NA}) is defined by:

$$\theta_{NA} = \sin^{-1} \left(\frac{NA}{n_{core}} \right) \quad (6)$$

The condition for TIR can be alternatively described by the critical angle θ_c (where $\theta_c = 90^\circ - \theta_{NA}$). Figure 7g geometrically

depicts these relationships using values from a reported elastomeric waveguide with polyurethane (PU) core ($n_{core} = 1.49$) and polydimethylsiloxane (PDMS) cladding ($n_{cladding} = 1.41$) used *in vivo*.^[114] For this waveguide, $NA = 0.48$ and $\theta_{NA} = 19^\circ$ ($\theta_c = 71^\circ$), meaning light rays with incident angles $< 19^\circ$ relative to the fiber axis can undergo TIR, while those with larger angles will be lost. Equation (5) also only applies to straight waveguides. Bends further decrease NA for a given material combination. Efficient waveguiding therefore relies on maximizing the RI contrast between core and cladding, particularly for flexible waveguides in which bends are inevitable. In designing waveguides for *in vivo* use, the determination of RI should also account for the use scenario; in the case of hydrogel waveguides, the relevant RIs are those of the swollen state hydrogels.^[115]

Waveguides can also be constructed from a single material, in which case waveguiding is dependent on the RI of the surroundings which effectively act as cladding. In implanted waveguides, the surroundings are the biological tissue, whose RI can vary from 1.33 to 1.51 depending on the tissue type.^[33] The waveguide RI therefore needs to exceed this value in order for TIR to occur, which can present an issue, particularly for hydrogel waveguides. The RI of hydrogels decreases approximately linearly from ≈ 1.54 for the constituent polymer network in the dry state to ≈ 1.34 at very high water content,^[33] and the RI of compliant hydrogels containing high water contents can be easily exceeded by tissue. Although the majority of optical waveguides for *in vivo* use are therefore core–cladding designs, some single material waveguides have proven effective *in vivo*,^[116] particularly if side emission via light leakage along the waveguide is favorable.^[117]

4.1.2. Optical Transparency

In addition to the extrinsic losses associated with the waveguide design, intrinsic optical losses occur through absorption and scattering within the waveguide material. The transmittance requirements to achieve light delivery on the centimeter scale for biomedical purposes can be achieved by a relatively wide range of biomaterials with attenuation coefficients $\approx 1 \text{ dB cm}^{-1}$ ($L_e \approx 4 \text{ cm}$) or better (Figure 8a).^[118] Off-target phototoxicity^[114] and heating^[34] from leaked light can nonetheless be an issue in some sensitive tissues, demanding better light confinement by limiting scattering in particular.

From a materials selection perspective, attenuation in silica optical fibers used for long-haul telecommunications ($\alpha = 0.2 \text{ dB km}^{-1}$ at 1550 nm) is several orders of magnitude lower than in polymeric optical fibers made from PMMA (0.15 dB m^{-1}) or polycarbonate (PC) (1 dB m^{-1}) at 520–780 nm,^[119] while biomaterials waveguides exhibit minimum attenuation values around 0.1 dB cm^{-1} ($L_e \approx 43 \text{ cm}$) and more typically around 1 dB cm^{-1} ($L_e \approx 4 \text{ cm}$) at vis wavelengths (Figure 8a). From a processing perspective, thermoplastics and hydrogels can require particular conditions for transparency. Scattering in waveguides made from semi-crystalline polymers like some thermoplastic polyesters is mostly suppressed by rapid cooling from the melt to avoid formation of crystallites.^[116] Alternatively, isomers or other comonomers built into the polymer backbone reduce crystallinity, like in poly(D,L-lactide) (PDLLA),^[120] poly(lactide-co-glycolide) (PLGA), and other polylactide (PLA)-based copolymers,^[121] with the additional advantage of easier processing at lower temperatures by thermal drawing^[120] or extrusion.^[121] For hydrogel waveguides, transparency is dictated by the polymer backbone composition, molar mass, crosslinking density, and water mass fraction. PEGDAs in particular are prevalent synthetic hydrogels used for biomedical waveguides, and compositions for optical transparency have been systematically evaluated.^[118] At polymer contents $\leq 50\%$ w/v, 500 Da PEGDA hydrogels are opaque, with optical loss of $\approx 25 \text{ dB cm}^{-1}$ ($L_e \approx 1.8 \text{ mm}$) at vis wavelengths, while polymer contents $\geq 60\%$ w/v give transparent gels with optical losses $< 0.2 \text{ dB cm}^{-1}$. PEGDA 700 Da hydrogels perform similarly.^[122] The opacity at lower polymer contents arises through polymerization-induced phase separation, in which the water content exceeds the equilibrium water uptake of the forming crosslinked network, creating micron-sized water-rich pores that scatter light.^[123] Although PEGDA 500 and 700 Da gels are transparent above 60% w/v, deformation and cracking upon swelling can occur at higher polymer contents.^[122] As a guideline, 60% w/v is a good compromise between optical transparency and only moderate swelling in low molar mass PEGDA hydrogels. During network formation, higher molar mass PEGDA is better able to accommodate high water contents without undergoing phase separation. At a polymer content of 10% w/v, bulk optical losses of 2, 5, and 10 kDa PEGDA hydrogels were 0.68 dB cm^{-1} ($L_e = 6.4 \text{ cm}$), 0.23 dB cm^{-1} ($L_e = 19 \text{ cm}$), and 0.17 dB cm^{-1} ($L_e = 26 \text{ cm}$) respectively in the 450–550 nm wavelength range.^[124] The transparency of natural polymer hydrogels is also influenced by polymer content. Calcium-crosslinked

alginate (Ca-alginate) for example is a natural polymer commonly employed as biocompatible cladding for waveguides intended for in vivo use. The transparency of alginate decreases with increasing concentration; optical loss at 400 nm increases from $\approx 0.5 \text{ dB cm}^{-1}$ at 1% w/v to $\approx 5 \text{ dB cm}^{-1}$ at 4% w/w.^[118] Inhomogeneities were visible under a microscope in 4% w/w Ca-alginate, meaning that scattering is the likely cause of loss. The use of Ca-alginate as waveguide cladding is therefore usually limited in the range of 0.5 to 2% w/w to reduce losses at the core-cladding interface.

4.1.3. Mechanical Properties

Ideally, the mechanical properties of an implanted waveguide will match those of the surrounding tissue. The stiffness values of reported implantable waveguide materials span many orders of magnitude (Figure 8b), with a strong recent trend toward more compliant, stretchable materials due to their better compatibility with soft tissue. At the top end of the stiffness range are waveguides made from silica, whose high modulus ($E \approx 70 \text{ GPa}$)^[125] and low elongation at break ($< 1\%$)^[126] have long been recognized as significant drawbacks for in vivo use due to inflexibility and potential breakage in soft tissue. PMMA^[127] and polyesters such as poly(L-lactide) (PLLA)^[116] offer Young's moduli $\approx 3 \text{ GPa}$, tensile strengths $\approx 70 \text{ MPa}$, and elongations at break of a few percent. These thermoplastics are therefore modestly more compliant than silica. Regenerated silk fibroin—with the regeneration process involving degumming, rehydration, and dialysis to remove the inflammatory sericin component^[128]—presents a natural alternative to synthetic thermoplastics, displaying comparable stiffness, extensibility, and toughness ($\approx 3 \text{ MJ m}^{-3}$)^[129] and low optical loss (0.25 dB cm^{-1} , $L_e = 17.4 \text{ cm}$ at 633 nm).^[130] Intact natural silk fibers are more extensible (4–16%), stronger (tensile strength $> 500 \text{ MPa}$), and tougher (70 MJ m^{-3}) than regenerated silk waveguides, but optical losses are an order of magnitude higher due to scattering from sidewall debris and twists.^[131] Improved toughness ($> 50 \text{ MJ m}^{-3}$), extensibility (35%), and strength ($\approx 170 \text{ MPa}$) can be imparted to regenerated silk fibroin materials by uniaxial extension,^[129] and could be explored for producing tougher silk fibroin waveguides with true elastomeric properties emulating those of native silk fibers.

More compliant, stretchable in vivo waveguides with Young's moduli in the low MPa range have been produced from elastomers based on polysiloxanes,^[132] PUs,^[114] and citrate-based polyesters.^[133] PDMS for example has a rich history as a biomaterial due to its biocompatibility, inertness, moldability on the sub-micron scale, and oxygen permeability,^[134] and its high transparency across the vis spectrum is appealing for stretchable waveguides. Core-cladding designs are accessible by tailoring the crosslinking degree to attain different RIs.^[135] Hydrogel-based waveguides are highly compliant and match the stiffness range of soft tissue ($E < 1 \text{ kPa}$ up to 5 MPa),^[136] and can be produced by chemical or physical crosslinking. Order-of-magnitude increases in strength, elongation, and toughness can be accessed by producing interpenetrating networks^[137] which enhance energy dissipation without substantially affecting stiffness.^[136] Step-index

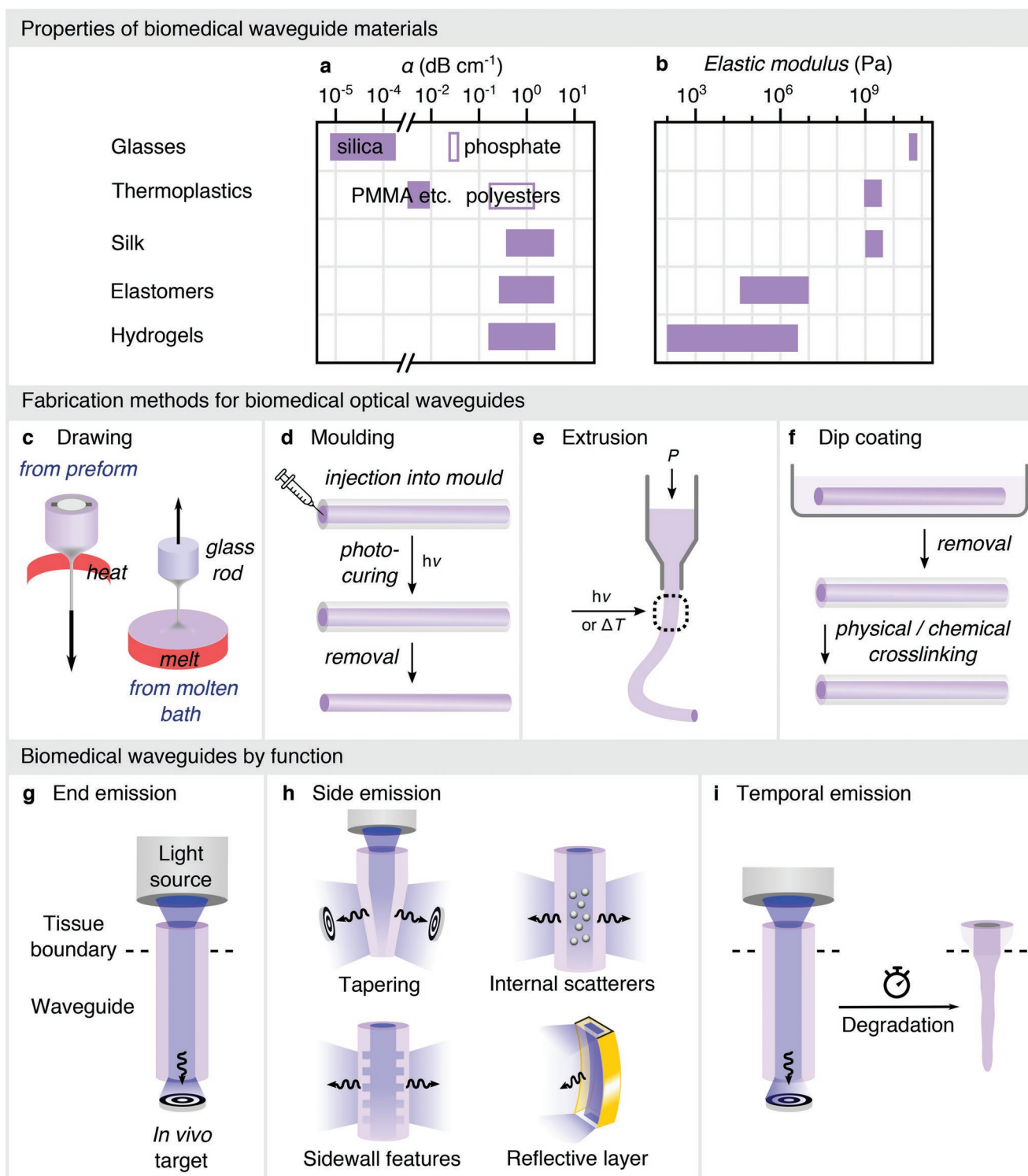


Figure 8. Comparison of the a) optical and b) mechanical properties of the main material classes demonstrated for biomedical waveguides. c–f) Fabrication technologies for biomedical waveguides. g–i) Overview of waveguide designs for in vivo light delivery.

hydrogel waveguides fabricated from double networks of polyacrylamide (PAM) and Ca-alginate exhibited tough, highly elastic mechanical properties with $E \approx 80$ kPa, elongation of 730%, and a failure stress of 230 kPa.^[138]

4.2. Fabrication Technologies for In Vivo Waveguides

There are three main processing technologies that have been employed to fabricate in vivo waveguides—drawing, molding,

and extrusion (Figure 8c–e).^[111b] Dip coating is a fourth technique that is commonly used to introduce cladding to a pre-formed core material (Figure 8f). Below we highlight the key features and selection criteria for each technology.

4.2.1. Drawing

In vivo cylindrical waveguides made from meltable materials, such as silica glass and thermoplastics, have largely been drawn from the melt at elevated temperature. Single material fibers of other thermoplastic materials can be drawn from a molten bath,^[116] while core–cladding fibers, some with complex internal structures, are drawn from preform rods already displaying the desired configuration of materials (Figure 8c).^[139] This process, which is also used to produce commercial optical fibers, involves heating a section of the preform in a furnace compartment of a drawing tower, applying axial tension so that the material flows, and collecting the resulting fiber which has a diameter typically >100-fold smaller than that of the preform. Cooling of the fiber as it moves out of the heated zone brings it below the glass transition temperature T_g and locks the dimensions, which are typically in the hundreds-of-microns diameter range. Smaller diameters, down to the tens-of-microns range, can be attained by a second drawing step.^[140] In some cases, the rapid cooling is also essential for the optical transparency of the material. Drawing of PLLA fibers from the melt, for example, suppressed crystallization through rapid cooling, which maximized light transmittance by avoiding scattering from crystalline domains.^[116] The recent use of patterned rollers to emboss nano- and micro-patterns onto the outer surface of drawn fibers offers further customizability of fiber geometry^[141] for controlled side emission. Although rare, drawing has also been reported for chemically crosslinked PDMS fibers from a partially-cured PDMS precursor bath.^[142] For fiber waveguides made from meltable materials, thermal drawing is a relatively straightforward approach that offers cheap production and high scalability that can produce hundreds or thousands of meters of drawn fiber per preform.^[143] The integration of additional functionalities (metal electrodes,^[144] hollow microfluidic channels^[145]) is also supported. The need for controlled heating and careful optimization of drawing conditions to attain specific fiber dimensions and optical properties are disadvantages, and the spatial positioning of different components (e.g., multiple waveguiding cores, conductive electrodes) is on the tens-of-microns scale. Microfabrication techniques can nonetheless be used to expose micron-resolution windows in the cladding material for precise side emission.^[146] All aspects of multimaterial fiber production have been recently reviewed by Sorin and co-workers.^[147]

4.2.2. Molding

Molding is the most popular choice for producing compliant elastomeric and hydrogel-based waveguides at the laboratory scale, utilizing in situ chemical or physical crosslinking. Reactive precursors are injected into the mold, which can be a cylindrical tube (for optical fibers), rectangular prism (for slab waveguides), or more complex form (e.g., for ridges), and then crosslinked

(Figure 8d). Molding has been used to produce rigid waveguides from silk^[148] and PLLA,^[117] elastomers based on PDMS,^[149] PU,^[114] and citrate-containing polyesters,^[133] and hydrogel waveguides based on PEGDA,^[124] PAM,^[150] agarose,^[151] and silk.^[148] Molding of synthetic hydrogel waveguides has predominantly employed transparent molds and photoinitiation^[124] or more rarely redox initiation^[150] to cure vinyl-containing precursors via radical polymerization. Hydrogel fibers of diameters < 100 μm have been reported using the molding approach.^[150] Molded elastomeric waveguides have been typically crosslinked by thermal curing of reactive precursors.^[133] Materials suitable for thermal drawing can in principle also be molded, with a comb-shaped PLLA waveguide, for example, produced by melt pressing to a thin film then laser cutting to shape,^[117] and a PLA microneedle array with overhead focusing lenses was melt molded using a PDMS template.^[152] Finally, molding can also be used to produce waveguides through drying of a precursor solution to give physically crosslinked materials. Silk waveguides in particular have been produced by casting aqueous solutions of regenerated silk fibroin^[153] or organic solutions of recombinant spider silk protein^[154] into molds followed by drying, with silk offering the possibility of producing surface features down to the nanoscale.^[155] On the other hand, unwanted surface roughness can be inherited from the mold and increase extrinsic optical loss.^[115,154,156] The molding approach is also a batchwise, single material process. Molding of core–cladding structures, for example, requires sequential molding steps which can be tedious.^[148] Removal of the formed waveguide from the mold is also required at the end of the process, which in the case of hydrogel-based optical fibers, has been achieved by swelling the silicone mold in organic solvent and using water pressure to eject the waveguide.^[118] These additional steps, particularly when involving organic solvent, are disadvantages of the molding process.

4.2.3. Extrusion

Extrusion is a relatively underutilized approach for in vivo waveguide fabrication, but can produce more complex structures (e.g., core–cladding fibers and non-cylindrical profiles) than drawing, while offering greater simplicity and scalability than molding. Extrusion can be applied to meltable and chemically- or physically-curable materials provided that the structural locking of the waveguide form—for example, through cooling below T_g or crosslinking—can be rapidly induced immediately after extrusion (Figure 8e). Extrusion has also been used for producing complex pre-forms, for example oversized hollow-channel pre-forms of resorbable glasses,^[157] that then undergo thermal drawing to generate the final waveguide. Our workgroup recently used extrusion-based printing processes to produce degradable polyester waveguides extruded from the melt,^[121] and degradable PEG-based hydrogel waveguides^[158] and non-degradable PDMS-based elastomeric waveguides cured by in situ photocrosslinking. Coaxial needles permitted core–cladding designs, avoiding the need to add the cladding post-fabrication. Coaxial extrusion of two thermoplastic PU elastomers has also been used to produce core–cladding elastomeric waveguides in a continuous and scalable manner,^[148] overcoming the low-throughput and tedious nature of molding

processes typically used to produce silicone-based elastomeric waveguides.^[159] Silk optical fibers have been produced by direct ink writing of aqueous silk fibroin into a methanol-rich coagulation bath.^[130] Extrusion offers relatively straightforward and scalable access to well-defined waveguide structures and further developments are likely as in vivo waveguide production adopts innovations from the booming 3D (bio)printing field.^[160]

4.2.4. Dip Coating

Dip coating is a common method for introducing a cladding layer to single-material waveguide cores. The pre-formed waveguide is dipped into a low-viscosity precursor solution of the cladding material, which is then cured by physical or chemical crosslinking (Figure 8f). Hydrogels are the most favored cladding materials introduced by dip coating, since they offer low RIs, compliance, flexibility, and high biocompatibility. Ca-alginate is a very popular natural polymer hydrogel cladding introduced by dipping into a solution of Na-alginate (e.g., 1% w/v) then dipping in a solution of CaCl_2 (e.g., 0.1 M) for physical crosslinking.^[156] Dip coating is relatively straightforward and versatile, since its application is relatively independent of the material and fabrication method of the pre-formed waveguide,^[116] but it does increase the number of fabrication steps. As more complex in vivo waveguides become accessible through single-step processes such as extrusion, the prevalence of dip coating is likely to decline.

4.3. Waveguides Discussed by Function

Several waveguide designs (Figure 8g–i) have been used to perform in vivo photoactivations described in Section 3.3. The simplest end emission design allows illumination of an in vivo target at the distal end of the waveguide (Figure 8g), employed mainly for optogenetics. Typically, low optical loss will be desirable to irradiate exclusively at the target site. The maximum illumination zone is then dictated by the cross-sectional area of the waveguide and the penetration of the light into the target zone. For illumination of larger tissue volumes or defined points along the waveguide, a side-emission design can be employed (Figure 8h), in which light out-coupling is controlled by introducing a taper, sidewall features, internal scatterers, or reflective layers. Side-emission waveguides have been utilized for neuronal optogenetics across larger brain areas, non-neuronal optogenetic therapies, PDT, and photochemical crosslinking of tissue. Degradable waveguides can be used for temporal illumination (Figure 8i) while avoiding a second surgical procedure to remove the waveguide post-treatment. Degradable versions of both end- and side-emission waveguides have been reported.

4.3.1. In Vivo Point Activation with End Emission Waveguides

The most straightforward use of waveguides is to act as a light conduit to the distal end (Figure 8g), which has been employed in biomedical scenarios such as optogenetics and therapies. Individual multimode silica fibers were used in

early optogenetic studies in live mice for light stimulation,^[161] before multifunctional waveguides predominated.^[162] To transition from silica to more compliant materials, Anikeeva and co-workers developed a series of flexible, multifunctional end-emitting waveguides with PC cores and cyclic olefin copolymer claddings by thermal drawing.^[139,145,163] The reasonably high optical transparency (e.g., $\alpha = 1.6\text{--}2.4\text{ dB cm}^{-1}$, $L_e = 2.7\text{--}1.8\text{ cm}$ at 473 nm)^[145] has allowed delivery of 300–400 mW cm^{-2} at the tip of 5 cm fibers fed with <1 mW of laser power to successfully excite optogenetically-engineered neurons in the brains or spinal cords of mice. Functional performance and biocompatibility was confirmed over 2 months, with lower glial scarring than in other chronically implanted probes attributed to the lower bending stiffness than silica. Hydrogel-based step-index optical fibers have been demonstrated as even more compliant waveguides for end emission in vivo.^[156] A PEGDA 700 Da (90% w/v)/Ca-alginate core-cladding fiber was used to deliver 560 and 640 nm light to deep tissue in live mice but without performing photoactivation. The low attenuation ($\alpha = 0.42\text{ dB cm}^{-1}$, $L_e = 10.3\text{ cm}$) permitted organ-scale light delivery. Optical fibers made entirely of highly stretchable PAM/Ca-alginate double network hydrogels ($E \approx 60\text{ kPa}$, $\alpha = 0.25\text{ dB cm}^{-1}$, $L_e \approx 174\text{ cm}$ at 472 nm in air) have also been used for optogenetic stimulation mice.^[150] After 4 weeks, the device showed unchanged performance, transparency, and stretchability, and significantly better tissue compatibility than a silica fiber control.

The target irradiation volume for end emission optical fibers is limited by the fiber cross-sectional area and light attenuation in tissue. Light emitted at 76 W cm^{-2} , for example, can achieve sufficient irradiance for optogenetics down to just 330 microns below the waveguide tip.^[162] Waveguides that exhibit multiple end-emitting zones have therefore been developed to allow irradiation of larger volumes or multiple locations. An optical microneedle array molded from PLLA was developed by Yun and co-workers as a waveguiding patch to deliver 491 nm blue light subcutaneously for antibacterial treatment.^[152] Each needle (1.6 mm long, 1 mm apart) in the 11×11 array acted as an individual waveguide, with a matching microlens array on the top surface of the device focusing light into each needle. When irradiated at the skin exposure limit, the device could deliver 50 J cm^{-2} —the fluence required to eliminate pathogenic drug-resistant bacteria—to a target depth of 2.5 mm, which was ninefold higher than the fluence achieved at that depth using direct skin irradiation. A similar microneedle array coupled with an LED light source was recently proposed for UV-based treatment of skin lesions in the deep dermis.^[164] Arrays of end-emitting optical fibers have also been developed for studying connectivity between different brain regions by optogenetics.^[165] A helical sheath was used to insert multiple fibers into an expanding radial pattern that placed their tips $\approx 1\text{ mm}$ apart in the mouse brain, allowing optical stimulation at disparate points.

4.3.2. In Vivo Multipoint or Large Volume Activation by Side Emission Waveguides

Side emitting waveguides can be used for spatially-defined activation at multiple discrete points or activation of large tissue

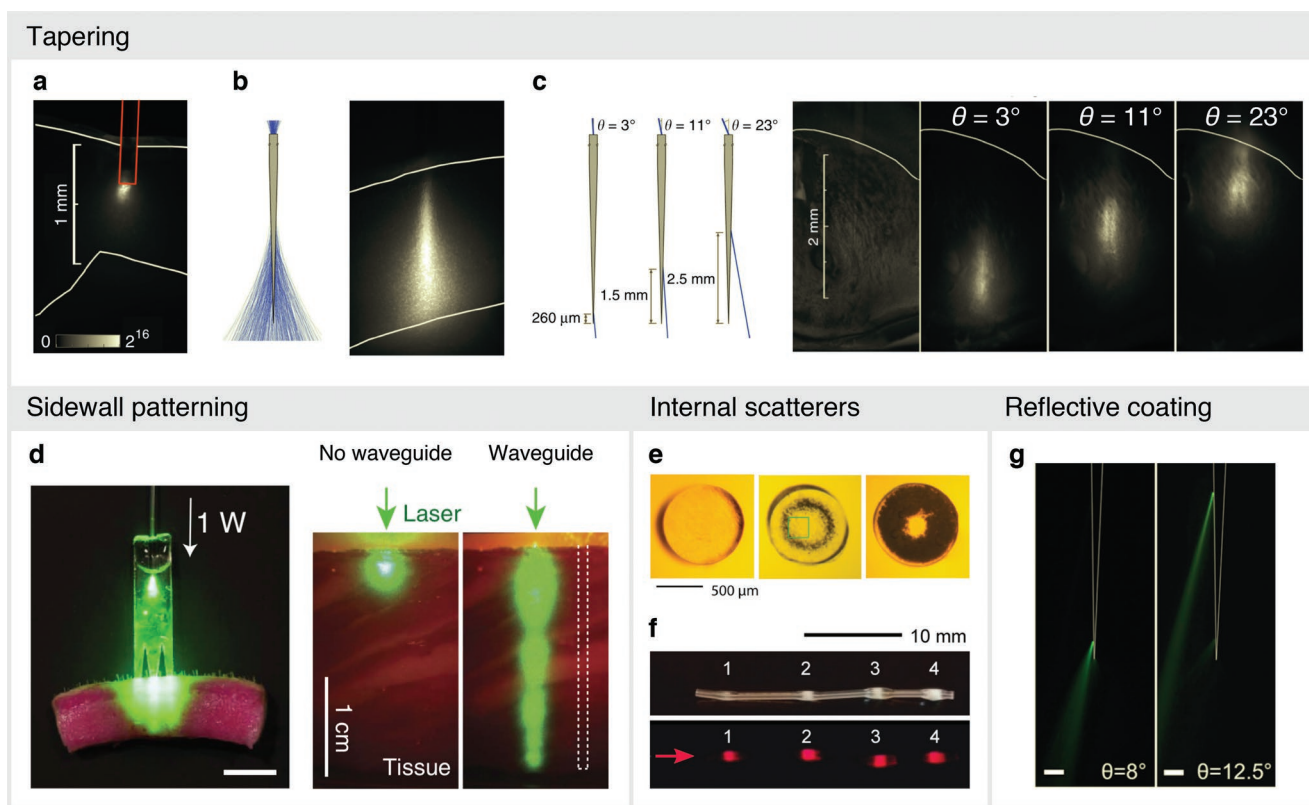


Figure 9. Side-emission waveguides. a) A flat-cleaved fiber shows low light penetration depth in a fluorescently-stained brain slice, compared with b) the extended emission profile expected from a tapered fiber into which light is in-coupled using the full NA of the fiber. c) The depth of an emission spot from the taper tip could be varied based on the in-coupling angle of single rays, allowing site-specific illumination within brain tissue (scale same as in (a)). Adapted with permission.^[166] Copyright 2017, Nature Publishing Group. d) Degradable, fork-shaped slab waveguide used for photochemical tissue bonding (PTB), with sidewall patterning and geometry allowing consistent side-emission intensity down to several centimeters in porcine tissue. Scale bar = 1 cm. Reproduced with permission.^[177] Copyright 2016, Nature Publishing Group. e) Microbubbles with increasing size (left to right) could be introduced into PES optical fibers by controlled heating at 200 °C for increasing number of seconds, with f) side-emission spots with increasing microbubble size (1–4) giving consistent out-coupled intensity of 633 nm light propagating along the fiber. Adapted with permission.^[169] Copyright 2019, Optical Society of America. g) Precisely micromachined windows in a reflective gold layer coated on tapered silica fibers. Scale bars = 100 μm. Reproduced with permission.^[177] Copyright 2014, Elsevier.

areas. The four main reported side emission designs are depicted in Figure 8h.

Tapering is one approach for controlled out-coupling of light along a waveguide axis. Pisanello and co-workers produced tapered silica waveguides by careful thermal drawing. Compared with flat-cleaved fibers that showed very low penetration depths (Figure 9a), tapered fibers were capable of both homogeneous and spatially-confined illumination over path lengths up to ≈1.8 mm for optogenetics in mouse brains.^[166] Light emission from the entire taper length was accessible by injecting all light angles accepted by the NA (Figure 9b), while site-selective illumination could be achieved by in-coupling specific incident angles (Figure 9c) which depart from the taper at predictable, well-defined positions in brain tissue, allowing selective triggering of different locomotion behavior in moving mice by irradiating distinct sub-regions of the striatum. In later work, larger illumination lengths of up to ≈3 mm were accessible by increasing the NA of the tapered waveguides to 0.66, which also allowed simultaneous illumination of two different regions of brain with different wavelengths of light (473 and 561 nm) using a single waveguide.^[167] Similar tapered waveguides were

used for optogenetic stimulation of a large volume of frontal eye field neurons in live non-human primates.^[34] Each of these examples used thermal drawing to introduce tapers of defined dimensions. The potential for tapering to improve the profile (e.g., uniformity) of side emission has also been demonstrated in more compliant side emission waveguides,^[149] and we expect will become more prevalent as waveguide fabrication methods (particularly for compliant materials) continue to develop.

Surface patterning is a second approach for controlled light out-coupling, which involves introducing a particular topology to the sidewalls of the waveguide during fabrication. The sidewall pattern presents angles that are not conducive to TIR, meaning that light can escape the waveguide. Clinical implementation of PDT in deep tumors has often exploited silica optical fibers fitted with commercially-available diffusing tips that generate uniform side emission over a defined length through controlled sidewall roughness.^[101] Sidewall patterning has been introduced via laser cutting onto a degradable, thin slab waveguide made of PLGA for example.^[117] The fork-shaped waveguide (Figure 9d) was inserted into centimeter-deep wounds for photochemical tissue bonding (PTB), which

involves light-induced crosslinking of PS-loaded tissue surfaces. The high optical loss of $\approx 10 \text{ dB cm}^{-1}$ in the waveguide was optimal for out-coupling $\approx 90\%$ of the light along its length to the surrounding tissue, allowing PTB at much greater depth than the current clinical treatment of directly irradiating superficial wounds. The waveguide gave sixfold greater adhesion strength versus the waveguide-free control in an ex vivo tissue model, extending the utility of PTB and showing promise for other light-based therapies requiring large irradiation areas. A related approach of introducing controlled variations in RI of the waveguide core along the propagating direction can offer very even side emission,^[168] and could be explored for in vivo waveguides if fabrication methods permit.

Introducing scattering species in the core of the waveguide is a third method for achieving side emission. We are not aware of in vivo waveguides employing this approach, but the principle has been demonstrated using polyethersulfone (PES) optical fibers produced by thermal drawing of water-free PES rods.^[169] The ability of PES to absorb up to 2% w/w water was exploited to vaporize nanopores of absorbed liquid water by briefly heating above T_g (e.g., for several seconds at 140–200 °C), which introduced microbubbles in the heated region. The microbubble cavities promoted scattering due to their lower RI, giving controlled side emission with losses in the waveguide of up to $\approx 2 \text{ dB cm}^{-1}$ ($L_e \approx 2 \text{ mm}$) at 633 nm depending on bubble diameter (Figure 9e,f). PES, however, is not an ideal waveguide material since the water nanopores already cause significant scattering losses at shorter vis (and UV) wavelengths, explaining why 633 nm light (optical loss $\approx 0.8 \text{ dB cm}^{-1}$, $L_e \approx 5.4 \text{ cm}$) was used in this work. Introducing side-scattering cavities or particles with precise spatial control into more transparent biomaterials is therefore an enticing target for bringing such side emission waveguides to in vivo use.

The out-coupling of light from unwanted regions of a waveguide can be entirely suppressed by the addition of a reflective layer. Yun and co-workers designed elastomeric waveguides to wrap around the equator of ex vivo rabbit eyes for the photochemical crosslinking of sclera collagen, which is a promising strategy for halting myopia—a cause of glaucoma and retinal detachment—in human patients.^[114] Ribbon-shaped core-clad waveguides with commercial PU elastomer core and PDMS cladding were produced by mold casting, and three of the faces were coated with a $<200 \text{ nm}$ thick reflective silver layer to restrict light out-coupling to the therapeutic side facing the sclera ($\alpha = 0.57 \text{ dB cm}^{-1}$, $L_e \approx 7.7 \text{ cm}$). Without this layer, bending would encourage light out-coupling^[170] predominantly toward the (unwanted) outside of the bend, potentially damaging the retina ($E_{\text{max}} = 0.1 \text{ mW cm}^{-2}$ for 445 nm light)^[38] if just a small fraction of light leaked. Irradiation from a CW diode laser (445 nm, 7 mW cm^{-2} , 1 h, $E/E_{\text{max}} \approx 0.1$) was delivered to riboflavin-treated sclera tissue, resulting in crosslinking that doubled the Young's modulus versus non-irradiated controls. The compliance and geometry of the elastomeric waveguide were key to correct positioning under the ocular muscles without causing mechanical damage. The uniformity of side emission irradiance (22% variation around the eye circumference) could be further improved by tapering.^[149] The reflective layer of a waveguide can also be precisely milled to introduce precise windows down to the nanoscale for site-selective out-coupling. Tapered silica fibers

coated with gold could be milled by focused ion beam to introduce side-emission windows which could be independently fed by choosing specific in-coupling light angles (Figure 9g), allowing optogenetic stimulation at specific depths with independent wavelengths.^[171] For a similar purpose, laser-cut windows ($20 \mu\text{m} \times 20 \mu\text{m}$) were introduced into waveguide claddings to allow side emission at multiple points spanning the cortex, hippocampus, and thalamus of live mice.^[146] Microfabrication approaches to introduce side-emission domains can involve hours of manual work using expensive equipment, with the cost per fiber estimated at USD 1000.^[171]

4.3.3. Temporal Emission Using Degradable Waveguides

Degradability is an important consideration in biomaterial design, with resorbable materials preferred in applications where light delivery is only needed during a certain time period and removal would be problematic (Figure 8i). Reported examples of degradable waveguides for biomedical applications include Ca-phosphate glasses,^[172] silk,^[148] cellulose butyrate,^[173] PLLA^[116] and polyester copolymers,^[121,164] polydioxanone,^[174] citrate-based polyester elastomers,^[133] and very recently, a degradable PEG-based hydrogel.^[158]

Phosphate-based glasses have been used extensively in biomedical applications since the early 1980s,^[175] offering degradation times ranging from days to years.^[176] With elastic moduli around 50 GPa,^[177] resorbable glasses do not solve the stiffness-related biocompatibility issues of silica waveguides, but they do avoid the need for surgical removal post-treatment while exhibiting good optical transparency from UV to NIR wavelengths. Ca-phosphate-based optical fibers with core-cladding structure were synthesized by thermal drawing of pre-formed rods above T_g ($\approx 440 \text{ °C}$).^[178] The core and cladding had only slightly different RIs (≈ 1.52) giving a low NA of 0.087 at 633 nm. Optical loss was 4.67 dB m^{-1} ($L_e = 93 \text{ cm}$) at 633 nm, and high biocompatibility and degradation were demonstrated over several months in rats.^[172] Core-cladding fibers with larger cores ($200 \mu\text{m}$) and NAs (0.17) have been more recently reported,^[179] moving resorbable glass waveguides closer to in vivo photoactivation.

Silk proteins are natural degradable materials with high transparency, excellent biocompatibility, and similar stiffness to thermoplastics. Biomedical devices made from solid regenerated silkworm silk degrade by enzymatic cleavage resulting in surface erosion, with degradation taking months to a year depending on the preparation technique and device geometry.^[180] Water annealing of silk devices encourages crystallization to β -sheet secondary structure which slows degradation.^[181] Solid silk fibroin exhibits relatively high optical clarity and RI (≈ 1.54),^[130] robust mechanical properties,^[182] and an amenity to form smooth interfaces, making it highly suitable for fabricating implantable optical devices.^[180] Silk optical waveguides have been prepared by printing a concentrated aqueous silk fibroin ink (30% w/w) through a $5 \mu\text{m}$ nozzle into a methanol-rich bath to encourage rapid solidification via β -sheet formation.^[130] The waveguides exhibited relatively low loss ($\alpha \approx 0.25 \text{ dB cm}^{-1}$, $L_e = 174 \text{ cm}$ at 633 nm on glass) but were not free standing, which limited applicability. A core-cladding alternative was produced in an all-aqueous process by evaporating

silk fibroin in a long narrow strip (40 μm \times 2.9 mm \times 9 cm) mold to form the core, then forming a silk fibroin hydrogel cladding in a second molding step.^[148] Relatively high optical loss ($\alpha \approx 2 \text{ dB cm}^{-1}$, $L_e \approx 2.2 \text{ cm}$ at 540 nm) was attributed to rough core edges, but still permitted light delivery around corners through centimeters of ex vivo muscle tissue. Recombinant spider silk waveguides have shown higher surface smoothness after molding, twofold higher resistance to mechanical buckling, twofold lower attenuation in ex vivo muscle tissue, and lower in vivo inflammatory response compared with regenerated silkworm silk,^[154] offering a degradable waveguide material with potentially enhanced all round performance.^[183]

Waveguide-assisted tissue bonding in deep wounds is a highly appropriate application of degradable waveguides (made from PLGA) discussed in the last section,^[117] since removal of a non-degradable waveguide would interfere with wound healing. Degradable PLLA-based waveguides have also shown utility for temporal optogenetics in live mice.^[116] A 220-micron diameter core-cladding fiber was produced by thermal drawing at 220 °C, giving $\alpha = 1.6 \text{ dB cm}^{-1}$ ($L_e \approx 2.7 \text{ cm}$) at 473 nm. Degradation studies in PBS showed that the surface roughness increased in the first 7 days, then stayed relatively constant for 4 weeks as the material switched from surface to bulk erosion. The waveguides could deliver 473 nm light (13 mW, 2 min pulses) to hippocampus neurons and trigger seizures in the animals on day 1, but diminished effects at day 3 and no effect at day 10 confirmed waveguide degradation, while silica fiber controls showed stable function over the same time period. As described earlier, the tendency of PLLA to crystallize, which would cause unwanted scattering, was suppressed in this case by rapid cooling during the fiber drawing process, but can also be avoided by using intrinsically amorphous polyesters, many of which are clinically approved for in vivo use^[184] and can be processed into waveguides at much lower temperatures.^[185] Recently, our workgroup reported a series of amorphous polyester waveguides produced from PDLA, PLGA, and PLA-co-PCL (PCL = polycaprolactone) using simple extrusion printing at <100 °C and moderate pressures (20–600 kPa).^[121] The polymers have T_g around body temperature, and waveguides were therefore soft and flexible under near-physiological conditions. Efficient waveguiding was demonstrated in tissue, with $\alpha = 0.14\text{--}0.44 \text{ dB cm}^{-1}$ ($L_e = 10\text{--}31 \text{ cm}$) at 405–520 nm. The PLA-co-PCL waveguide showed particularly high flexibility and efficient light guiding at low bending radii due to its lower T_g of 18 °C. 405 nm light could be delivered across 8 cm of ex vivo muscle tissue with sufficient irradiance at the distal end ($\approx 30 \text{ mW cm}^{-2}$) to trigger cell migration in a photoresponsive hydrogel bearing photoprotected cell-adhesive ligands, highlighting the potential of the fibers for biomaterial activation in deep tissue. Although complete degradation may take months, it is important to recognize that light attenuation in degradable polyester waveguides such as PDLA can increase dramatically ($>1 \text{ dB cm}^{-1}$) within an hour of immersion.^[185]

Citrate-based elastomers are degradable alternatives to silicones, offering high transparency, widely tunable stiffnesses (<1 kPa to MPa) and degradation rates (days to years), and well-established biocompatibility.^[186] Shan et al.^[133] developed a step-index optical fiber from two biocompatible citrate-based elastomers for organ-scale light delivery and detection.

The poly(octamethylene citrate) cladding was synthesized by thermal crosslinking of a pre-polymer melt around a removable template, then poly(octamethylene maleate citrate) pre-polymer was filled and crosslinked in the core. The multiple high temperature processes with multi-day curing times are drawbacks of the approach. Fibers exhibited stiffness $\approx 3.4 \text{ MPa}$, tensile strength $\approx 1.3 \text{ MPa}$, and elongation $\approx 60\%$, with the RI difference of ≈ 0.003 ($NA \approx 0.1$) sufficient for waveguiding to give $\alpha = 0.4 \text{ dB cm}^{-1}$ ($L_e \approx 11 \text{ cm}$) at 633 nm. Excitation of a fluorescent gel embedded in rat belly demonstrated the potential for deep tissue activation in vivo. The mechanical properties and degradation on the month timescale are suitable for high strain in vivo activation where temporal light delivery is required.

Degradable hydrogels are widely used for soft tissue regeneration,^[187] and are appealing as high compliance temporal waveguides. Natural polymer hydrogels, which exhibit high water contents and therefore low RIs that can be exceeded by tissue, are more suitable as degradable cladding materials for in vivo waveguides, while synthetic hydrogel cores have to date been non-degradable. We recently reported degradable synthetic hydrogel waveguides made from PEGDA-based prepolymers.^[158] The prepolymers contained thioether groups which accelerate hydrolysis of the adjacent ester functions in resulting hydrogels. Optical fibers were produced by extrusion printing of prepolymer solutions using in situ UV crosslinking, with increasing prepolymer molar masses resulting in declining stiffnesses (from 23 to 0.14 MPa), increasing elongations ($>30\%$), increasing swelling ratios (from 73% to 540%), and decreasing degradation times (from months to weeks) in resulting fibers. The relatively low optical losses ($\alpha < 0.4 \text{ dB cm}^{-1}$, $L_e > 11 \text{ cm}$ at 520 nm) allowed efficient light delivery through many centimeters of ex vivo porcine tissue to trigger cell migration in a light-responsive hydrogel and stimulate drug secretion from optogenetically-engineered bacteria in a living biomaterial. Core-cladding structures with acrylated Pluronic F127 cladding could also be printed using a coaxial needle, which further reduced optical losses by protecting the compliant core from bending losses observed when in direct contact with tissue. Although the in vivo application of these materials needs to be demonstrated, the combination of tunable mechanics, degradability with waveguiding performance makes them interesting in multiple scenarios.

4.4. Conclusions and Outlook on Waveguides

Waveguides offer a clear path for photoactivation of in vivo targets at centimeter-scale depths and minimize unwanted exposure of surrounding tissue to stray photons. From the materials perspective, the recent trend is toward compliant and/or degradable materials to maximize compatibility with soft tissue and to avoid the need for post-treatment removal. Hydrogels are at the forefront of biomedical waveguiding materials, and are highly relevant for combining with photoactivatable hydrogel-based biomaterials since they can also incorporate living cells. Other compliant materials such as elastomers and flexible thermoplastics are also growing in prominence for photoactivation in soft tissue. Degradable waveguides are particularly interesting for temporal light delivery in the body, and the

further development of waveguide materials that offer tailored degradation profiles may open new therapeutic possibilities. Future degradable waveguides may also incorporate bioactive species for release during degradation,^[188] such as viral vectors embedded in silk for one-step optogenetic transfection and waveguide implantation.^[189]

From the fabrication perspective, methods such as extrusion printing offer more convenient production of compliant waveguides than established batch-wise processes. We expect that further advances in (bio)printing techniques can be transferred to waveguide fabrication, permitting introduction of additional functional materials that serve purposes beyond waveguiding. Compliant side emission fibers could introduce additional materials or sidewall patterning during fabrication to encourage spatially-controlled outcoupling of light. Thermally drawn fibers have already transitioned from simple single material fibers to complex multicomponent fibers incorporating electrodes^[139,145,150,163] and hollow microfluidic channels^[145,162,163b] that are suitable for precise optogenetic studies without needing expensive microfabrication techniques. Developing convenient production methods to combine multiple waveguiding portions and additional component for electrical, optical, and microfluidic delivery and detection in hydrogel waveguides would be highly valuable. Such waveguides could be interfaced with photoactivatable biomaterials for all-in-one photoactivation, monitoring, and delivery of bioactive agents. Examples in which waveguides are integrated with photoactivatable biomaterials, for example, the cell-laden hydrogel as an optogenetic drug delivery device, are rare. The new field of living (bio)materials, which incorporates living cells that serve therapeutic or diagnostic functions into supportive materials, offers exciting prospects for combining waveguiding functionality with living photoactive targets for therapy. It is hoped that the examples for in vivo photoactivation that have been presented here stimulate further development of photoactivatable biomaterials in which waveguiding is an intrinsic element of the device design.

5. Overall Conclusions and Perspectives

The successful translation of photoactivatable biomaterials to the clinic requires robust light delivery methods to overcome light attenuation by tissue and associated photodamage. With the majority of photoresponsive groups requiring UV and short vis wavelengths, direct 1P photoactivation through tissue is restricted to hundreds-of-microns depth while respecting MPE for human skin. Red-shifted 1P-active groups modestly extend workable in vivo activation depth at the expense of complicated syntheses and solubility challenges. 2P-responsive groups are NIR activatable but require high powered pulsed lasers that are hard to employ clinically. Materials-based strategies are highly promising alternatives to significantly increase the activation depth without needing sophisticated hardware or integrated power sources such as in implantable LEDs developed for optogenetics. UCNP extend workable photoactivation depths to several centimeters using low-power NIR light sources, and waveguides can provide a clear path for organ-scale light delivery independent of wavelength. Materials capable of SHG still require high powered pulsed lasers but may be useful in

some niche scenarios. This review has highlighted the successful implementation of these materials-based light management strategies in the key application areas of optogenetics, drug delivery, regenerative medicine, and PDT. Quantification of light doses and photoactivation depths provide clear guidance for extending the approaches to upcoming photoresponsive biomaterials.

The photoresponsive biomaterials field and others requiring light delivery, for example, optogenetics will continue to benefit from innovations in the light delivery materials themselves. Improving the brightness of UCNP and the SHG efficiency of non-centrosymmetric materials while honoring biocompatibility requirements of the constituent materials will continue to offer greater direct path photoactivation depths. Producing waveguides with mechanical properties tailored to the intended tissue environment and excellent optical properties will be the focus of waveguide development. Waveguides that offer precisely-controlled side emission profiles and degradation profiles optimized for the use scenarios are both in focus. Improving light guiding properties by enhancing material homogeneity, surface smoothness, core-cladding design, and light in-coupling are goals that need to be tackled by optimizing fundamental properties of the waveguiding materials and improving fabrication methods. Nanotechnologists, materials scientists, and engineers have opportunities to progress these methods that can then be uptaken for photoactivation of biomaterials. Nonetheless, we see direct involvement and collaboration with the photoresponsive biomaterials community as the most efficient path toward clinical applications.

The merging of light delivery functions with photoresponsive biomaterials to form integrated devices is the first highly promising option for fast-tracking in vivo implementation. As both the light delivery and the photoresponsive target are materials-based, the expertise to construct both functions is often in the same workgroup, and can be implemented from the beginning of the device design. The incorporation of UCNP into photoactivatable hydrogels for regenerative purposes, for example, does not require additional processing technologies if the UCNP are already in hand. Additive technologies such as extrusion-based printing methods offer possibilities to build multicomponent devices comprising of distinct upconversion, waveguiding, and/or photoresponsive domains. Hydrogel-based waveguides are particularly promising for this purpose, as they can be produced by 3D (bio)printing and host bioactive species and living cells suitable for non-neuronal optogenetic treatments and tissue regeneration. Precisely compartmentalized waveguiding and photoreponsive components may also be augmented with optical/electrical sensing and microfluidic delivery in a similar manner to recent thermally-drawn multifunctional waveguides for optogenetics.

Combining distinct technologies developed for “direct path” and “clearing the path” photoactivations offers further opportunities to improve light delivery to deep tissue targets. The transparent nature of UCNP-containing silica microneedles has already been shown to assist in NIR delivery to the UCNP for optogenetic stimulation at low NIR irradiances.^[40] The integration of UCNP or SHG-capable (nano)materials into waveguides is a promising option for deep UV/vis photochemistry by guiding NIR photons to the embedded transducing materials.

Full integration of such light delivery functions with photoreponsive biomaterials themselves is an enticing prospect.

As the improvements in the design of photoactivatable materials and their integration with light management technologies enhances therapeutic potential, the step to clinical translation moves closer. Clinical translation of light-based therapies requires proof of safety across the entire device function including the delivered light energy, the photoresponsive material, and any materials used to assist in light delivery. Systems that include optogenetically living components, such as photoresponsive living therapeutic materials, face further regulatory hurdles related to the presence of genetically-modified organisms. Safety of UCNP has yet to be fully proven, with researchers seeking standardization of synthesis, characterization, and toxicity testing protocols to help bridge the gap between laboratory research and clinical application. From the waveguiding side, selected materials mostly focus on materials approved for clinical use, which facilitate their translation from a regulatory standpoint. Light management technologies that deliver photons more efficiently combined with photoactivatable materials that can respond to lower irradiances will increase the likelihood of photoactivation at safe light doses, but phototoxicity still needs to be assessed for each application scenario. Despite these challenges, we see a bright future for the clinical adoption of photoresponsive biomaterials facilitated by new and emerging light management technologies.

Acknowledgements

S.P. and A.d.C. received funding from the European Union's Horizon 2020 research and innovation program under the FET PROACTIVE grant agreement no. 731957 (Mechano-Control). J.F. acknowledges financial support from the China Scholarship Council (CSC).

Open access funding enabled and organized by Projekt DEAL.

Conflict of Interest

The authors declare no conflict of interest.

Keywords

biomaterials, photoactivation, photoresponsive, upconversion nanoparticles, waveguides

Received: June 21, 2021

Revised: August 24, 2021

Published online:

- [1] a) L. Beaute, N. McClenaghan, S. Lecommandoux, *Adv. Drug Delivery Rev.* **2019**, 138, 148; b) W. Zhao, Y. Zhao, Q. Wang, T. Liu, J. Sun, R. Zhang, *Small* **2019**, 15, 1903060.
- [2] W. He, M. Reaume, M. Hennenfent, B. P. Lee, R. Rajachar, *Biomater. Sci.* **2020**, 8, 3248.
- [3] a) A. M. Kloxin, A. M. Kasko, C. N. Salinas, K. S. Anseth, *Science* **2009**, 324, 59; b) C. A. DeForest, K. S. Anseth, *Nat. Chem.* **2011**, 3, 925; c) D. R. Griffin, A. M. Kasko, *J. Am. Chem. Soc.* **2012**, 134, 13103; d) M. J. Salierno, A. J. García, A. del Campo, *Adv. Funct. Mater.* **2013**, 23, 5974.

- [4] M. Wu, X. Lin, X. Tan, J. Li, Z. Wei, D. Zhang, Y. Zheng, A.-x. Zheng, B. Zhao, Y. Zeng, X. Liu, J. Liu, *ACS Appl. Mater. Interfaces* **2018**, 10, 19416.
- [5] T. T. Lee, J. R. García, J. I. Paez, A. Singh, E. A. Phelps, S. Weis, Z. Shafiq, A. Shekaran, A. del Campo, A. J. García, *Nat. Mater.* **2015**, 14, 352.
- [6] S. He, J. Song, J. Qu, Z. Cheng, *Chem. Soc. Rev.* **2018**, 47, 4258.
- [7] T. L. Rapp, C. A. DeForest, *Adv. Healthcare Mater.* **2020**, 9, 1901553.
- [8] R. Weinstain, T. Slanina, D. Kand, P. Klán, *Chem. Rev.* **2020**, 120, 13135.
- [9] E. Palao, T. Slanina, L. Muchová, T. Šolomek, L. Vítek, P. Klán, *J. Am. Chem. Soc.* **2016**, 138, 126.
- [10] Q. Lin, L. Yang, Z. Wang, Y. Hua, D. Zhang, B. Bao, C. Bao, X. Gong, L. Zhu, *Angew. Chem., Int. Ed.* **2018**, 57, 3722.
- [11] M. Dong, A. Babalhavaej, S. Samanta, A. A. Beharry, G. A. Woolley, *Acc. Chem. Res.* **2015**, 48, 2662.
- [12] A. Chaudhuri, Y. Venkatesh, J. Das, K. K. Behara, S. Mandal, T. K. Maiti, N. D. P. Singh, *ACS Appl. Nano Mater.* **2018**, 1, 6312.
- [13] S. Samanta, A. A. Beharry, O. Sadovski, T. M. McCormick, A. Babalhavaej, V. Tropepe, G. A. Woolley, *J. Am. Chem. Soc.* **2013**, 135, 9777.
- [14] T. L. Rapp, C. B. Highley, B. C. Manor, J. A. Burdick, I. J. Dmochowski, *Chem. - Eur. J.* **2018**, 24, 2328.
- [15] Z. L. Rodgers, R. M. Hughes, L. M. Doherty, J. R. Shell, B. P. Molesky, A. M. Brugh, M. D. E. Forbes, A. M. Moran, D. S. Lawrence, *J. Am. Chem. Soc.* **2015**, 137, 3372.
- [16] A. Farrukh, J. I. Paez, A. del Campo, *Adv. Funct. Mater.* **2019**, 29, 1807734.
- [17] J.-H. Park, Z. Yu, K. Lee, P. Lai, Y. Park, *APL Photonics* **2018**, 3, 100901.
- [18] P. Gutruf, J. A. Rogers, *Curr. Opin. Neurobiol.* **2018**, 50, 42.
- [19] S. Gai, C. Li, P. Yang, J. Lin, *Chem. Rev.* **2014**, 114, 2343.
- [20] a) B. Yan, J.-C. Boyer, D. Habault, N. R. Branda, Y. Zhao, *J. Am. Chem. Soc.* **2012**, 134, 16558; b) Y. Yang, F. Liu, X. Liu, B. Xing, *Nanoscale* **2012**, 5, 231; c) P. T. Burks, J. V. Garcia, R. Gonzalez-Irias, J. T. Tillman, M. Niu, A. A. Mikhailovsky, J. Zhang, F. Zhang, P. C. Ford, *J. Am. Chem. Soc.* **2013**, 135, 18145; d) W. Li, J. Wang, J. Ren, X. Qu, *J. Am. Chem. Soc.* **2014**, 136, 2248; e) Y. Zheng, Z. Chen, Q. Jiang, J. Feng, S. Wu, A. del Campo, *Nanoscale* **2020**, 12, 13654.
- [21] S. Chen, A. Z. Weitemier, X. Zeng, L. He, X. Wang, Y. Tao, A. J. Y. Huang, Y. Hashimoto-dani, M. Kano, H. Iwasaki, L. K. Parajuli, S. Okabe, D. B. L. Teh, A. H. All, I. Tsutsui-Kimura, K. F. Tanaka, X. Liu, T. J. McHugh, *Science* **2018**, 359, 679.
- [22] H. Ye, M. D.-E. Baba, R.-W. Peng, M. Fussenegger, *Science* **2011**, 332, 1565.
- [23] C. Liu, Y. Zhang, M. Liu, Z. Chen, Y. Lin, W. Li, F. Cao, Z. Liu, J. Ren, X. Qu, *Biomaterials* **2017**, 139, 151.
- [24] Y. Zhang, K. Ren, X. Zhang, Z. Chao, Y. Yang, D. Ye, Z. Dai, Y. Liu, H. Ju, *Biomaterials* **2018**, 163, 55.
- [25] J.-J. Hu, Q. Lei, X.-Z. Zhang, *Prog. Mater. Sci.* **2020**, 114, 100685.
- [26] S. H. Yun, S. J. J. Kwok, *Nat. Biomed. Eng.* **2017**, 1, 0008.
- [27] S. Shabahang, S. Kim, S.-H. Yun, *Adv. Funct. Mater.* **2018**, 28, 1706635.
- [28] G.-H. Lee, H. Moon, H. Kim, G. H. Lee, W. Kwon, S. Yoo, D. Myung, S. H. Yun, Z. Bao, S. K. Hahn, *Nat. Rev. Mater.* **2020**, 5, 149.
- [29] S. Wen, J. Zhou, K. Zheng, A. Bednarkiewicz, X. Liu, D. Jin, *Nat. Commun.* **2018**, 9, 2415.
- [30] S. Wilhelm, *ACS Nano* **2017**, 11, 10644.
- [31] A. H. All, X. Zeng, D. B. L. Teh, Z. Yi, A. Prasad, T. Ishizuka, N. Thakor, Y. Hiromu, X. Liu, *Adv. Mater.* **2019**, 31, 1803474.
- [32] A. Alabugin, *Photochem. Photobiol.* **2019**, 95, 722.
- [33] S. L. Jacques, *Phys. Med. Biol.* **2013**, 58, R37.

- [34] L. Acker, E. N. Pino, E. S. Boyden, R. Desimone, *Proc. Natl. Acad. Sci. USA* **2016**, 113, E7297.
- [35] C. E. Tedford, S. DeLapp, S. Jacques, J. Anders, *Lasers Surg. Med.* **2015**, 47, 312.
- [36] a) W. A. Velema, W. Szymanski, B. L. Feringa, *J. Am. Chem. Soc.* **2014**, 136, 2178; b) M. Chen, J. Hu, L. Wang, Y. Li, C. Zhu, C. Chen, M. Shi, Z. Ju, X. Cao, Z. Zhang, *Sci. Rep.* **2020**, 10, 14447.
- [37] A. T. Hillel, S. Unterman, Z. Nahas, B. Reid, J. M. Coburn, J. Axelman, J. J. Chae, Q. Guo, R. Trow, A. Thomas, Z. Hou, S. Lichtsteiner, D. Sutton, C. Matheson, P. Walker, N. David, S. Mori, J. M. Taube, J. H. Elisseeff, *Sci. Transl. Med.* **2011**, 3, 93ra67.
- [38] International Commission on Non-Ionizing Radiation Protection, *Health Phys.* **2013**, 105, 271.
- [39] A. Schroeder, M. S. Goldberg, C. Kastrup, Y. Wang, S. Jiang, B. J. Joseph, C. G. Levins, S. T. Kannan, R. Langer, D. G. Anderson, *Nano Lett.* **2012**, 12, 2685.
- [40] Y. Wang, X. Lin, X. Chen, X. Chen, Z. Xu, W. Zhang, Q. Liao, X. Duan, X. Wang, M. Liu, F. Wang, J. He, P. Shi, *Biomaterials* **2017**, 142, 136.
- [41] R. S. Stern, K. T. Nichols, L. H. Väkevää, *N. Engl. J. Med.* **1997**, 336, 1041.
- [42] J. Liebmann, M. Born, V. Kolb-Bachofen, *J. Invest. Dermatol.* **2010**, 130, 259.
- [43] R. Prakash, O. Yizhar, B. Grewe, C. Ramakrishnan, N. Wang, I. Goshen, A. M. Packer, D. S. Peterka, R. Yuste, M. J. Schnitzer, K. Deisseroth, *Nat. Methods* **2012**, 9, 1171.
- [44] J. R. Bolton, *Photochem. Photobiol.* **2020**, 96, 1355.
- [45] P. Klán, T. Šolomek, C. G. Bochet, A. Blanc, R. Givens, M. Rubina, V. Popik, A. Kostikov, J. Wirz, *Chem. Rev.* **2013**, 113, 119.
- [46] B. F. Hochheimer, *Appl. Opt.* **1982**, 21, 1516.
- [47] Y. Guo, P. P. Ho, A. Tirkliunas, F. Liu, R. R. Alfano, *Appl. Opt.* **1996**, 35, 6810.
- [48] K. König, *J. Microsc.* **2000**, 200, 83.
- [49] M. D. Barnes, A. Mehta, T. Thundat, R. N. Bhargava, V. Chhabra, B. Kulkarni, *J. Phys. Chem. B* **2000**, 104, 6099.
- [50] G. Chen, H. Qiu, P. N. Prasad, X. Chen, *Chem. Rev.* **2014**, 114, 5161.
- [51] A. Nadort, V. K. A. Sreenivasan, Z. Song, E. A. Grebenik, A. V. Nechaev, V. A. Semchishen, V. Y. Panchenko, A. V. Zvyagin, *PLoS One* **2013**, 8, e63292.
- [52] C. Würth, M. Kaiser, S. Wilhelm, B. Grauel, T. Hirsch, U. Resch-Genger, *Nanoscale* **2017**, 9, 4283.
- [53] H. Ding, L. Lu, Z. Shi, D. Wang, L. Lia, X. Li, Y. Renb, C. Liu, D. Cheng, H. Kim, N. C. Giebink, X. Wang, L. Yin, L. Zhao, M. Luo, X. Sheng, *Proc. Natl. Acad. Sci. USA* **2018**, 115, 6632.
- [54] H. Schaefer, P. Ptacek, O. Zerzouf, M. Haase, *Adv. Funct. Mater.* **2008**, 18, 2913.
- [55] F. Wang, J. Wang, X. Liu, *Angew. Chem., Int. Ed.* **2010**, 49, 7456.
- [56] a) P. Yuan, Y. H. Lee, M. K. Gnanasammandhan, Z. Guan, Y. Zhang, Q.-H. Xu, *Nanoscale* **2012**, 4, 5132; b) Q. Lue, F. Guo, L. Sun, A. Li, L. Zhao, *J. Appl. Phys.* **2008**, 103, 123533.
- [57] X. Lin, X. Chen, W. Zhang, T. Sun, P. Fang, Q. Liao, X. Chen, J. He, M. Liu, F. Wang, P. Shi, *Nano Lett.* **2018**, 18, 948.
- [58] A. Pliss, T. Y. Ohulchanskyy, G. Chen, J. Damasco, C. E. Bass, P. N. Prasad, *ACS Photonics* **2017**, 4, 806.
- [59] Q. Zhan, J. Qian, H. Liang, G. Somesfalean, D. Wang, S. He, Z. Zhang, S. Andersson-Engels, *ACS Nano* **2011**, 5, 3744.
- [60] W. Zou, C. Visser, J. A. Maduro, M. S. Pshenichnikov, J. C. Hummelen, *Nat. Photonics* **2012**, 6, 560.
- [61] J. Shen, G. Chen, A.-M. Vu, W. Fan, O. S. Bilsel, C.-C. Chang, G. Han, *Adv. Opt. Mater.* **2013**, 1, 644.
- [62] X. Wu, Y. Zhang, K. Takle, O. Bilsel, Z. Li, H. Lee, Z. Zhang, D. Li, W. Fan, C. Duan, E. M. Chan, C. Lois, Y. Xiang, G. Han, *ACS Nano* **2016**, 10, 1060.
- [63] X. Lin, Y. Wang, X. Chen, R. Yang, Z. Wang, J. Feng, H. Wang, K. W. C. Lai, J. He, F. Wang, P. Shi, *Adv. Healthcare Mater.* **2017**, 6, 1700446.
- [64] S. W. Perry, R. M. Burke, E. B. Brown, *Ann. Biomed. Eng.* **2012**, 40, 277.
- [65] X. Chen, O. Nadiarynk, S. Plotnikov, P. J. Campagnola, *Nat. Protoc.* **2012**, 7, 654.
- [66] D. A. Dombeck, K. A. Kasischke, H. D. Vishwasrao, M. Ingelsson, B. T. Hyman, W. W. Webb, *Proc. Natl. Acad. Sci. USA* **2003**, 100, 7081.
- [67] T. Boulesteix, E. Beaupaire, M.-P. Sauviat, M.-C. Schanne-Klein, *Opt. Lett.* **2004**, 29, 2031.
- [68] V. Parodi, E. Jacchetti, R. Osellame, G. Cerullo, D. Polli, M. T. Raimondi, *Front. Bioeng. Biotechnol.* **2020**, 8, 585363.
- [69] A. Barhoumi, B. Salvador-Culla, D. S. Kohane, *Adv. Healthcare Mater.* **2015**, 4, 1159.
- [70] A. Rogov, Y. Mugnier, L. Bonacina, *J. Opt.* **2015**, 17, 033001.
- [71] G. Malkinson, P. Mahou, E. Chaudan, T. Gacoin, A. Y. Sonay, P. Pantazis, E. Beaupaire, W. Supatto, *ACS Photonics* **2020**, 7, 1036.
- [72] J. Riporto, M. Urbain, Y. Mugnier, V. Multian, F. Riporto, K. Bredillet, S. Beauquis, C. Galez, V. Monnier, Y. Chevrolot, V. Gayvoronsky, L. Bonacina, R. L. Dantec, *Opt. Mater. Express* **2019**, 9, 1955.
- [73] D. Staedler, T. Magouroux, R. Hadji, C. Joulaud, J. Extermann, S. Schwung, S. Passemand, C. Kasparian, G. Clarke, M. Germann, R. L. Dantec, Y. Mugnier, D. Rytz, D. Ciepielewski, C. Galez, S. Gerber-Lemaire, L. Juillerat-Jeanneret, L. Bonacina, J.-P. Wolf, *ACS Nano* **2012**, 6, 2542.
- [74] a) J. Vuilleumier, G. Gaulier, R. De Matos, D. Ortiz, L. Menin, G. Campargue, C. Mas, S. Constant, R. Le Dantec, Y. Mugnier, L. Bonacina, S. Gerber-Lemaire, *ACS Appl. Mater. Interfaces* **2019**, 11, 27443; b) J. Vuilleumier, G. Gaulier, R. D. Matos, Y. Mugnier, G. Campargue, J.-P. Wolf, L. Bonacina, S. Gerber-Lemaire, *Helv. Chim. Acta* **2020**, 103, 1900251.
- [75] K. Deisseroth, *Nat. Neurosci.* **2015**, 18, 1213.
- [76] R. Chen, A. Canales, P. Anikeeva, *Nat. Rev. Mater.* **2017**, 2, 16093.
- [77] J. Y. Lin, P. M. Knutsen, A. Muller, D. Kleinfeld, R. Y. Tsien, *Nat. Neurosci.* **2013**, 16, 1499.
- [78] N. C. Klapoetke, Y. Murata, S. S. Kim, S. R. Pulver, A. Birdsey-Benson, Y. K. Cho, T. K. Morimoto, A. S. Chuong, E. J. Carpenter, Z. Tian, J. Wang, Y. Xie, Z. Yan, Y. Zhang, B. Y. Chow, B. Surek, M. Melkonian, V. Jayaraman, M. Constantine-Paton, G. K.-S. Wong, E. S. Boyden, *Nat. Methods* **2014**, 11, 338.
- [79] W. Yang, L. Carrillo-Reid, Y. Bando, D. S. Peterka, R. Yuste, *eLife* **2018**, 7, 32671.
- [80] L. He, Y. Zhang, G. Ma, P. Tan, Z. Li, S. Zang, X. Wu, J. Jing, S. Fang, L. Zhou, Y. Wang, Y. Huang, P. G. Hogan, G. Han, Y. Zhou, *eLife* **2015**, 4, 10024.
- [81] A. Bohineust, Z. Garcia, B. Corre, F. Lemaître, P. Bousso, *Nat. Commun.* **2020**, 11, 1143.
- [82] X. Ai, L. Lyu, Y. Zhang, Y. Tang, J. Mu, F. Liu, Y. Zhou, Z. Zuo, G. Liu, B. Xing, *Angew. Chem., Int. Ed.* **2017**, 56, 3031.
- [83] E. Palao, T. Slanina, L. Muchova, T. Solomek, L. Vitek, P. Klan, *J. Am. Chem. Soc.* **2016**, 138, 126.
- [84] S. S. Said, S. Campbell, T. Hoare, *Chem. Mater.* **2019**, 31, 4971.
- [85] Y. Dai, H. Xiao, J. Liu, Q. Yuan, P. a. Ma, D. Yang, C. Li, Z. Cheng, Z. Hou, P. Yang, J. Lin, *J. Am. Chem. Soc.* **2013**, 135, 18920.
- [86] H. Kang, K. Zhang, Q. Pan, S. Lin, D. S. H. Wong, J. Li, W. Y.-W. Lee, B. Yang, F. Han, G. Li, B. Li, L. Bian, *Adv. Funct. Mater.* **2018**, 28, 1802642.
- [87] Y. Pan, J. Yang, X. Luan, X. Liu, X. Li, J. Yang, T. Huang, L. Sun, Y. Wang, Y. Lin, Y. Song, *Sci. Adv.* **2019**, 5, eaav7199.
- [88] G. C. J. Lindberg, K. S. Lim, B. G. Soliman, A. Nguyen, G. J. Hooper, R. J. Narayan, T. B. F. Woodfield, *Appl. Phys. Rev.* **2021**, 8, 011301.
- [89] H. Zhu, H. Yang, Y. Ma, T. J. Lu, F. Xu, G. M. Genin, M. Lin, *Adv. Funct. Mater.* **2020**, 30, 2000639.
- [90] R.-Z. Lin, Y.-C. Chen, R. Moreno-Luna, A. Khademhosseini, J. M. Melero-Martin, *Biomaterials* **2013**, 34, 6785.

- [91] J. C. J. Wei, G. A. Edwards, D. J. Martin, H. Huang, M. L. Crichton, M. A. F. Kendall, *Sci. Rep.* **2017**, 7, 15885.
- [92] J. Elisseeff, K. Anseth, D. Sims, W. McIntosh, M. Randolph, R. Langer, *Proc. Natl. Acad. Sci. USA* **1999**, 96, 3104.
- [93] a) J. Zhu, Q. Zhang, T. Yang, Y. Liu, R. Liu, *Nat. Commun.* **2020**, 11, 3462; b) Z. Chen, X. Wang, S. Li, S. Liu, H. Miao, S. Wu, *ChemPhotoChem* **2019**, 3, 1077.
- [94] N. B. Cramer, C. N. Bowman, in *Thiol-X Chemistries in Polymer and Materials Science*, Vol. 1 (Eds: A. Lowe, C. Bowman), Royal Society of Chemistry, Cambridge **2013**, p. 1.
- [95] a) A. Dobos, J. Van Hoorick, W. Steiger, P. Gruber, M. Markovic, O. G. Andriotis, A. Rohatschek, P. Dubruel, P. J. Thurner, S. Van Vlierberghe, S. Baudis, A. Ovsianikov, *Adv. Healthcare Mater.* **2019**, 9, 1900752; b) S. Chung, H. Lee, H.-S. Kim, M.-G. Kim, L. P. Lee, J. Y. Lee, *Nanoscale* **2016**, 8, 14213.
- [96] C. D. McNitt, H. Cheng, S. Ullrich, V. V. Popik, M. Bjerknes, *J. Am. Chem. Soc.* **2017**, 139, 14029.
- [97] R. Raman, T. Hua, D. Gwynne, J. Collins, S. Tamang, J. Zhou, T. Esfandiary, V. Soares, S. Pajovic, A. Hayward, R. Langer, G. Traverso, *Sci. Adv.* **2020**, 6, eaay0065.
- [98] S. Kwiatkowski, B. Knap, D. Przysupski, J. Saczko, E. Kędzierska, K. Knap-Czop, J. Kotlińska, O. Michel, K. Kotowski, J. Kulbacka, *Biomed. Pharmacother.* **2018**, 106, 1098.
- [99] S. S. Lucky, K. C. Soo, Y. Zhang, *Chem. Rev.* **2015**, 115, 1990.
- [100] F. Cieplik, D. Deng, W. Crielard, W. Buchalla, E. Hellwig, A. Al-Ahmad, T. Maisch, *Crit. Rev. Microbiol.* **2018**, 44, 571.
- [101] M. M. Kim, A. Darafsheh, *Photochem. Photobiol.* **2020**, 96, 280.
- [102] I. Yoon, J. Z. Li, Y. K. Shim, *Clin. Endosc.* **2013**, 46, 7.
- [103] S. Iinuma, K. T. Schomacker, G. Wagnieres, M. Rajadhyaksha, M. Bamberg, T. Momma, T. Hasan, *Cancer Res.* **1999**, 59, 6164.
- [104] B. W. Henderson, T. M. Busch, L. A. Vaughan, N. P. Frawley, D. Babich, T. A. Sosa, J. D. Zollo, A. S. Dee, M. T. Cooper, D. A. Bellnier, W. R. Greco, A. R. Oseroff, *Cancer Res.* **2000**, 60, 525.
- [105] Y. I. Park, H. M. Kim, J. H. Kim, K. C. Moon, B. Yoo, K. T. Lee, N. Lee, Y. Choi, W. Park, D. Ling, K. Na, W. K. Moon, S. H. Choi, H. S. Park, S.-Y. Yoon, Y. D. Suh, S. H. Lee, T. Hyeon, *Adv. Mater.* **2012**, 24, 5755.
- [106] a) Z. Hou, K. Deng, C. Li, X. Deng, H. Lian, Z. Cheng, D. Jin, J. Lin, *Biomaterials* **2016**, 101, 32; b) M. Sun, L. Xu, W. Ma, X. Wu, H. Kuang, L. Wang, C. Xu, *Adv. Mater.* **2016**, 28, 898.
- [107] M. Guan, H. Dong, J. Ge, D. Chen, L. Sun, S. Li, C. Wang, C. Yan, P. Wang, C. Shu, *NPG Asia Mater.* **2015**, 7, e205.
- [108] R. Lv, P. Yang, F. He, S. Gai, G. Yang, Y. Dai, Z. Hou, J. Lin, *Biomaterials* **2015**, 63, 115.
- [109] W. Fan, W. Bu, B. Shen, Q. He, Z. Cui, Y. Liu, X. Zheng, K. Zhao, J. Shi, *Adv. Mater.* **2015**, 27, 4155.
- [110] W. Fan, B. Shen, W. Bu, F. Chen, Q. He, K. Zhao, S. Zhang, L. Zhou, W. Peng, Q. Xiao, D. Ni, J. Liu, J. Shi, *Biomaterials* **2014**, 35, 8992.
- [111] a) J. Wang, J. Dong, *Sensors* **2020**, 20, 3981; b) R. Nazempour, Q. Zhang, R. Fu, X. Sheng, *Materials* **2018**, 11, 1283.
- [112] T. Brown, in *Fiber Optics Handbook: Fiber, Devices, and Systems for Optical Communications* (Eds: M. Bass, E. W. Van Stryland), McGraw-Hill, New York **2002**.
- [113] M. Pisanello, A. D. Patria, L. Sileo, B. L. Sabatini, M. D. Vittorio, F. Pisanello, *Biomed. Opt. Express* **2015**, 6, 4014.
- [114] S. J. J. Kwok, S. Forward, C. M. Wertheimer, A. C. Liapis, H. H. Lin, M. Kim, T. G. Seiler, R. Birngruber, I. E. Kochevar, T. Seiler, S.-H. Yun, *Invest. Ophthalmol. Visual Sci.* **2019**, 60, 2563.
- [115] J. Guo, X. Liu, N. Jiang, A. K. Yetisen, H. Yuk, C. Yang, A. Khademhosseini, X. Zhao, S. H. Yun, *Adv. Mater.* **2016**, 28, 10244.
- [116] R. Fu, W. Luo, R. Nazempour, D. Tan, H. Ding, K. Zhang, L. Yin, J. Guan, X. Sheng, *Adv. Opt. Mater.* **2018**, 6, 1700941.
- [117] S. Nizamoglu, M. C. Gather, M. Humar, M. Choi, S. Kim, K. S. Kim, S. K. Hahn, G. Scarcelli, M. Randolph, R. W. Redmond, S. H. Yun, *Nat. Commun.* **2016**, 7, 10374.
- [118] A. K. Yetisen, N. Jiang, A. Fallahi, Y. Montelongo, G. U. Ruiz-Esparza, A. Tamayol, Y. S. Zhang, I. Mahmood, S.-A. Yang, K. S. Kim, H. Butt, A. Khademhosseini, S.-H. Yun, *Adv. Mater.* **2017**, 29, 1606380.
- [119] N. Ioannides, E. B. Chunga, A. Bachmatiuk, I. G. Gonzalez-Martinez, B. Trzebiecka, D. B. Adebimpe, D. Kalymnios, M. H. Rummeli, *Mater. Res. Express* **2014**, 1, 032002.
- [120] A. Gierej, M. Vagenende, A. Filipkowski, B. Siwicki, R. Buczynski, H. Thienpont, S. Van Vlierberghe, T. Geernaert, P. Dubruel, F. Berghmans, *J. Light. Technol.* **2019**, 37, 1916.
- [121] J. Feng, Q. Jiang, P. Rogin, P. W. de Oliveira, A. del Campo, *ACS Appl. Mater. Interfaces* **2020**, 12, 20287.
- [122] J. Guo, M. Zhou, C. Yang, *Sci. Rep.* **2017**, 7, 7902.
- [123] Y.-H. Wu, H. B. Park, T. Kai, B. D. Freeman, D. S. Kalika, *J. Membr. Sci.* **2010**, 347, 197.
- [124] M. Choi, J. W. Choi, S. Kim, S. Nizamoglu, S. K. Hahn, S. H. Yun, *Nat. Photonics* **2013**, 7, 987.
- [125] G. B. Docker, *Appl. Opt.* **1979**, 18, 1445.
- [126] R. C. d. S. B. Allil, M. M. Werneck, *IEEE Trans. Instrum. Meas.* **2011**, 60, 2118.
- [127] M. K. Szczurowski, T. Martynkien, G. Statkiewicz-Barabach, L. Khan, D. J. Webb, C. Ye, J. Dulieu-Barton, W. Urbanczyk, *Proc. SPIE* **2010**, 7714, 77140G.
- [128] H. Perry, A. Gopinath, D. L. Kaplan, L. Dal Negro, F. G. Omenetto, *Adv. Mater.* **2008**, 20, 3070.
- [129] J. Yin, E. Chen, D. Porter, Z. Shao, *Biomacromolecules* **2010**, 11, 2890.
- [130] S. T. Parker, P. Domachuk, J. Amsden, J. Bressner, J. A. Lewis, D. L. Kaplan, F. G. Omenetto, *Adv. Mater.* **2009**, 21, 2411.
- [131] S. Kujala, A. Mannila, L. Karvonen, K. Kieu, Z. Sun, *Sci. Rep.* **2016**, 6, 22358.
- [132] J. Guo, B. Zhou, C. Yang, Q. Dai, L. Kong, *Adv. Funct. Mater.* **2019**, 29, 1902898.
- [133] D. Shan, C. Zhang, S. Kalaba, N. Mehta, G. B. Kim, Z. Liu, J. Yang, *Biomaterials* **2017**, 143, 142.
- [134] F. Abbasi, H. Mirzadeh, A.-A. Katbab, *Polym. Int.* **2001**, 50, 1279.
- [135] J. Missinne, S. Kalathimekkad, B. Van Hoe, E. Bosman, J. Vanfleteren, G. Van Steenberge, *Opt. Express* **2014**, 22, 4168.
- [136] P. Calvert, *Adv. Mater.* **2009**, 21, 743.
- [137] J. P. Gong, Y. Katsuyama, T. Kurokawa, Y. Osada, *Adv. Mater.* **2003**, 15, 1155.
- [138] J.-Y. Sun, X. Zhao, W. R. K. Illeperuma, O. Chaudhuri, K. H. Oh, D. J. Mooney, J. J. Vlassak, Z. Suo, *Nature* **2012**, 489, 133.
- [139] C. Lu, U. P. Froriep, R. A. Koppes, A. Canales, V. Caggiano, J. Selvidge, E. Bizzi, P. Anikeeva, *Adv. Funct. Mater.* **2014**, 24, 6594.
- [140] Y. Guo, C. F. Werner, A. Canales, L. Yu, X. Jia, P. Anikeeva, T. Yoshinobu, *PLoS One* **2020**, 15, 0228076.
- [141] Z. Wang, T. Wu, Z. Wang, T. Zhang, M. Chen, J. Zhang, L. Liu, M. Qi, Q. Zhang, J. Yang, W. Liu, H. Chen, Y. Luo, L. Wei, *Nat. Commun.* **2020**, 11, 3842.
- [142] I. Martincek, D. Pudis, M. Chalupova, *IEEE Photonics Technol. Lett.* **2014**, 26, 1446.
- [143] A. Canales, S. Park, A. Kilias, P. Anikeeva, *Acc. Chem. Res.* **2018**, 51, 829.
- [144] M. Du, L. Huang, J. Zheng, Y. Xi, Y. Dai, W. Zhang, W. Yan, G. Tao, J. Qiu, K.-F. So, C. Ren, S. Zhou, *Adv. Sci.* **2020**, 7, 2001410.
- [145] A. Canales, X. Jia, U. P. Froriep, R. A. Koppes, C. M. Tringides, J. Selvidge, C. Lu, C. Hou, L. Wei, Y. Fink, P. Anikeeva, *Nat. Biotechnol.* **2015**, 33, 277.
- [146] S. Jiang, D. C. Patel, J. Kim, S. Yang, W. A. Mills, Y. Zhang, K. Wang, Z. Feng, S. Vijayan, W. Cai, A. Wang, Y. Guo, I. F. Kimbrough, H. Sontheimer, X. Jia, *Nat. Commun.* **2020**, 11, 6115.

- [147] W. Yan, A. Page, T. Nguyen-Dang, Y. Qu, F. Sordo, L. Wei, F. Sorin, *Adv. Mater.* **2019**, *31*, 1802348.
- [148] M. B. Applegate, G. Perotto, D. L. Kaplan, F. G. Omenetto, *Biomed. Opt. Express* **2015**, *6*, 4221.
- [149] S. J. J. Kwok, M. Kim, H. H. Lin, T. G. Seiler, E. Beck, P. Shao, I. E. Kochevar, T. Seiler, S.-H. Yun, *Invest. Ophthalmol. Visual Sci.* **2017**, *58*, 2596.
- [150] L. Wang, C. Zhong, D. Ke, F. Ye, J. Tu, L. Wang, Y. Lu, *Adv. Opt. Mater.* **2018**, *6*, 1800427.
- [151] A. Jain, A. H. J. Yang, D. Erickson, *Opt. Lett.* **2012**, *37*, 1472.
- [152] M. Kim, J. An, K. S. Kim, M. Choi, M. Humar, S. J. J. Kwok, T. Dai, S. H. Yun, *Biomed. Opt. Express* **2016**, *7*, 4220.
- [153] B. D. Lawrence, M. Cronin-Golomb, I. Georgakoudi, D. L. Kaplan, F. G. Omenetto, *Biomacromolecules* **2008**, *9*, 1214.
- [154] X. Qiao, Z. Qian, J. Li, H. Sun, Y. Han, X. Xia, J. Zhou, C. Wang, Y. Wang, C. Wang, *ACS Appl. Mater. Interfaces* **2017**, *9*, 14665.
- [155] H. Tao, D. L. Kaplan, F. G. Omenetto, *Adv. Mater.* **2012**, *24*, 2824.
- [156] M. Choi, M. Humar, S. Kim, S.-H. Yun, *Adv. Mater.* **2015**, *27*, 4081.
- [157] D. Gallichi-Nottiani, D. Pugliese, N. G. Boetti, D. Milanese, D. Janner, *Int. J. Appl. Glass Sci.* **2020**, *11*, 632.
- [158] J. Feng, Y. Zheng, S. Bhusari, M. Villiou, S. Pearson, A. del Campo, *Adv. Funct. Mater.* **2020**, *30*, 2004327.
- [159] J. Guo, M. Niu, C. Yang, *Optica* **2017**, *4*, 1285.
- [160] a) X. Cui, J. Li, Y. Hartanto, M. Durham, J. Tang, H. Zhang, G. Hooper, K. Lim, T. Woodfield, *Adv. Healthcare Mater.* **2020**, *9*, 1901648; b) Z. Jiang, B. Diggle, M. L. Tan, J. Viktorova, C. W. Bennett, L. A. Connal, *Adv. Sci.* **2020**, *7*, 2001379.
- [161] A. M. Aravanis, L.-P. Wang, F. Zhang, L. A. Meltzer, M. Z. Mogri, M. B. Schneider, K. Deisseroth, *J. Neural Eng.* **2007**, *4*, S143.
- [162] H. Shin, Y. Son, U. Chae, J. Kim, N. Choi, H. J. Lee, J. Woo, Y. Cho, S. H. Yang, C. J. Lee, I.-J. Cho, *Nat. Commun.* **2019**, *10*, 3777.
- [163] a) C. Lu, S. Park, T. J. Richner, A. Derry, I. Brown, C. Hou, S. Rao, J. Kang, C. T. Moritz, Y. Fink, P. Anikeeva, *Sci. Adv.* **2017**, *3*, 1600955; b) S. Park, Y. Guo, X. Jia, H. K. Choe, B. Grena, J. Kang, J. Park, C. Lu, A. Canales, R. Chen, *Nat. Neurosci.* **2017**, *20*, 612.
- [164] H. Zhang, H. B. Zhao, X. Y. Zhao, C. K. Xu, D. Franklin, A. Vazquez-Guardado, W. B. Bai, J. Zhao, K. Li, G. Monti, W. Lu, A. Kobeissi, L. M. Tian, X. Ning, X. G. Yu, S. Mehta, D. Chanda, Y. G. Huang, S. Xu, B. E. P. White, J. A. Rogers, *Adv. Funct. Mater.* **2021**, *31*, 2100576.
- [165] A. N. Zorzos, E. S. Boyden, C. G. Fonstad, *Opt. Lett.* **2010**, *35*, 4133.
- [166] F. Pisanello, G. Mandelbaum, M. Pisanello, I. A. Oldenburg, L. Sileo, J. E. Markowitz, R. E. Peterson, A. Della Patria, T. M. Haynes, M. S. Emara, B. Spagnolo, S. R. Datta, M. De Vittorio, B. L. Sabatini, *Nat. Neurosci.* **2017**, *20*, 1180.
- [167] M. Pisanello, F. Pisano, L. Sileo, E. Maglie, E. Bellistri, B. Spagnolo, G. Mandelbaum, B. L. Sabatini, M. De Vittorio, F. Pisanello, *Sci. Rep.* **2018**, *8*, 4467.
- [168] Z. Pan, L. Wondraczek, *Sci. Rep.* **2018**, *8*, 9527.
- [169] S. Shabahang, S. Forward, S.-H. Yun, *Opt. Express* **2019**, *27*, 7560.
- [170] R. T. Schermer, J. H. Cole, *IEEE J. Quantum Electron.* **2007**, *43*, 899.
- [171] F. Pisanello, L. Sileo, I. A. Oldenburg, M. Pisanello, L. Martiradonna, J. A. Assad, B. L. Sabatini, M. De Vittorio, *Neuron* **2014**, *82*, 1245.
- [172] O. Podrazký, P. Peterka, I. Kašík, S. Vytýkáčová, J. Probošťová, J. Mrázek, M. Kuneš, V. Závalová, V. Radochová, O. Lyutakov, E. Ceci-Ginistrelli, D. Pugliese, N. G. Boetti, D. Janner, D. Milanese, *J. Biophotonics* **2019**, *12*, 201800397.
- [173] A. Dupuis, N. Guo, Y. Gao, N. Godbout, S. Lacroix, C. Dubois, M. Skorobogatiy, *Opt. Lett.* **2007**, *32*, 109.
- [174] W. J. Choi, K. S. Park, B. H. Lee, *J. Biomed. Opt.* **2014**, *19*, 090503.
- [175] J. Burnie, T. Gilchrist, S. Duff, C. Drake, N. Harding, A. Malcolm, *Biomaterials* **1981**, *2*, 244.
- [176] a) B. C. Bunker, G. W. Arnold, J. A. Wilder, *J. Non-Cryst. Solids* **1984**, *64*, 291; b) P. Lopez-Iscua, N. Ojha, D. Pugliese, A. Mishra, R. Gumenyuk, N. G. Boetti, D. Janner, J. Troles, B. Bureau, C. Boussard-Plédel, J. Massera, D. Milanese, L. Petit, *J. Am. Ceram. Soc.* **2019**, *102*, 6882.
- [177] V. M. Sglavo, D. Pugliese, F. Sartori, N. G. Boetti, E. Ceci-Ginistrelli, G. Franco, D. Milanese, *J. Alloys Compd.* **2019**, *778*, 410.
- [178] E. Ceci-Ginistrelli, D. Pugliese, N. G. Boetti, G. Novajra, A. Ambrosone, J. Lousteau, C. Vitale-Brovarone, S. Abrate, D. Milanese, *Opt. Mater. Express* **2016**, *6*, 2040.
- [179] L. D. Sieno, N. G. Boetti, A. D. Mora, D. Pugliese, A. Farina, S. K. V. Sekar, E. Ceci-Ginistrelli, D. Janner, A. Pifferi, D. Milanese, *J. Biophotonics* **2018**, *11*, 201600275.
- [180] H. Tao, J. M. Kainerstorfer, S. M. Siebert, E. M. Pritchard, A. Sassaroli, B. J. B. Panilaitis, M. A. Brenckle, J. J. Amsden, J. Levitt, S. Fantini, *Proc. Natl. Acad. Sci. USA* **2012**, *109*, 19584.
- [181] X. Hu, K. Shmelev, L. Sun, E.-S. Gil, S.-H. Park, P. Cebe, D. L. Kaplan, *Biomacromolecules* **2011**, *12*, 1686.
- [182] C. Jiang, X. Wang, R. Gunawidjaja, Y. H. Lin, M. K. Gupta, D. L. Kaplan, R. R. Naik, V. V. Tsukruk, *Adv. Funct. Mater.* **2007**, *17*, 2229.
- [183] K. H. Tow, D. M. Chow, F. Vollrath, I. Dicaire, T. Gheysens, L. Thévenaz, *J. Lightwave Technol.* **2017**, *36*, 1138.
- [184] I. Manavitehrani, A. Fathi, H. Badr, S. Daly, A. Negahi Shirazi, F. Dehghani, *Polymers* **2016**, *8*, 20.
- [185] A. Gieriej, A. Filipkowski, D. Pysz, R. Buczynski, M. Vagenende, P. Dubruel, H. Thienpont, T. Geernaert, F. Berghmans, *J. Light. Technol.* **2020**, *38*, 1905.
- [186] M. Mehdizadeh, H. Weng, D. Gyawali, L. Tang, J. Yang, *Biomaterials* **2012**, *33*, 7972.
- [187] N. Annabi, A. Tamayol, J. A. Uquillas, M. Akbari, L. E. Bertassoni, C. Cha, G. Camci-Unal, M. R. Dokmeci, N. A. Peppas, A. Khademhosseini, *Adv. Mater.* **2014**, *26*, 85.
- [188] Z. Zhou, Z. Shi, X. Cai, S. Zhang, S. G. Corder, X. Li, Y. Zhang, G. Zhang, L. Chen, M. Liu, *Adv. Mater.* **2017**, *29*, 1605471.
- [189] S. L. Jackman, C. H. Chen, S. N. Chettih, S. Q. Neufeld, I. R. Drew, C. K. Agba, I. Flaquer, A. N. Stefano, T. J. Kennedy, J. E. Belinsky, K. Roberston, C. C. Beron, B. L. Sabatini, C. D. Harvey, W. G. Regehr, *Cell Rep.* **2018**, *22*, 3351.



Samuel Pearson obtained his Ph.D. in Polymer Chemistry from CAMD (UNSW, Australia) in 2014, before conducting postdoctoral projects at the C2P2 group (Lyon, France) working on nanocomposites and at the IPREM (Pau, France) as an MSCA Individual Fellow developing light-responsive surfaces. He is now Head of Applications in the Dynamic Biomaterials group at the Leibniz Institute for New Materials (INM) led by Prof. Aránzazu del Campo. His research focuses on hydrogels for 3D cell encapsulation and for delivering light inside the body, with an emphasis on technology transfer.



Jun Feng received his B.S. and M.S. degrees from Wuhan University of Technology, China in 2011 and 2015 before moving to Germany for his Ph.D. under the supervision of Prof. Aránzazu del Campo at the Leibniz Institute for New Materials (INM). His Ph.D., completed in 2020, focused on extrusion printing of biomedical optical waveguides based on compliant, degradable materials including hydrogels. He is now a postdoctoral researcher in the group of Prof. Rainer Haag at Freie Universität Berlin, developing hydrogels for antiviral applications, especially for SARS-CoV-2.



Aránzazu del Campo is Scientific Director of INM-Leibniz Institute for New Materials and Professor for Materials Synthesis at Saarland University (Germany) since 2015. Her group exploits synthetic phototriggers and photoresponsive biological processes to design instructive microenvironments that can guide cell behavior in vitro and in vivo using light. She studied Chemistry and obtained her Ph.D. in Polymer Science in 2000 at the Instituto de Ciencia y Tecnología de Polimeros (Madrid, Spain). After postdoctoral stays in Germany and Italy, she initiated her independent career in 2004 at the Max-Planck Institute for Metal Research followed by the Max-Planck Institute for Polymer research.